Title

Targeting microglial MyD88 reprograms injury-activated microglia and promotes spinal cord repair via TGF-β signaling and biomimetic nanodelivery

Authors

Jintao Liu[1,2,3,4a], Beibei Yu[5a], Wanjun Cao[2,3a], Jilu Liu[4a], Yundi Gao[6], Honghui Mao[2,3], Xiaochuan Gao[2,3], Lingli Guo[1], Shengyou Li[1], Qiao Huang[2,3], Mingze Qin[1], Fang Kuang[2,3]*, Jinghui Huang[1]*

Affiliations

[1]*Department of Orthopedics, Xijing Hospital, Fourth Military Medical University, Xi'an 710032, China*

[2]*Department of Neurobiology, School of Basic Medicine, Fourth Military Medical University, Xi'an 710032, China*

[3]*The Shaanxi Province Key Laboratory of Brain Function Analysis and Modulation, Xi'an 710032, China*

[4]*Department of Orthopedics, Naval Hospital of Eastern Theater, Zhoushan 316000, China*

[5]*Department of Neurosurgery, The First Affiliated Hospital of Chongqing Medical University, Chongqing, 400016, China*

[6]*Seventh Squad, Second Regiment, Basic Medical College, Fourth Military Medical University, Xi'an 710032, China*

*Corresponding authors at: No. 169, Changle West Road, Xi'an, China (F.K.);
No. 127, Changle West Road, Xi'an 710032, China (J.H.).
*Address correspondence to: Email: kuangf@fmmu.edu.cn (F.K.);
huangjh@fmmu.edu.cn (J.H.).
a These authors contributed equally to this work.

Abstract

Background: Following spinal cord injury (SCI), activated microglia sustain neuroinflammation and drive secondary tissue damage, and this limits functional recovery. Myeloid differentiation primary response 88 (MyD88) is a central adaptor of innate immune signaling, but whether and how microglial MyD88 regulates state transition after SCI remains unclear. This study aims to explore the impact of microglial MyD88 signaling on microglial state trajectories and tissue repair after SCI and to develop a microglia-targeted delivery strategy for therapeutic modulation.

Methods: A forceps-mediated SCI mouse model was established, and bulk and single-cell RNA sequencing were used to profile the temporal activation of microglial MyD88 signaling in the spinal cord. Pharmacological MyD88 inhibition (ST2825) and inducible microglia-specific MyD88 conditional knockout mice (*Tmem119*^{CreERT2};*Myd88*$^{fl/fl}$) were used to assess neuroinflammation, tissue remodeling and downstream signaling. Functional recovery was evaluated by behavioral testing, bidirectional axonal tracing and electrophysiology. For translational validation, microglia membrane-coated, peptide-modified biomimetic nanoparticles

(ST2825·DSPE@MG) were engineered to enhance microglia targeting and therapeutic efficacy.

Results: Transcriptomic analyses revealed rapid and sustained activation of MyD88 signaling preferentially in microglia after SCI. ST2825 suppressed pro-inflammatory outputs *in vitro* and *in vivo* while preserving trophic mediators. Microglia-specific MyD88 deletion reprogrammed injury-activated microglia from a pro-inflammatory state to a repair-associated phenotype, reducing neuronal damage, preserving axons and improving locomotor recovery. TGF-β receptor blockade with LY2109761 abolished the protective effects of MyD88 deficiency. Additionally, ST2825·DSPE@MG nanoparticles exhibited microglia-targeted uptake and conferred superior therapeutic efficacy.

Conclusion: Our data establish MyD88 as a critical regulator of microglial reprogramming after SCI and highlight its potential as a therapeutic target for spinal cord repair.

Keywords

MyD88; microglial state transition; spinal cord injury; TGF-β; biomimetic nanoparticle

Introduction

Spinal cord injury (SCI) initiates an immediate mechanical insult followed by a prolonged secondary injury cascade [1]. This secondary phase, characterized by sustained neuroinflammation, oxidative stress and scar formation, contributes to long-term neurological deficits and limits endogenous repair capacity [2, 3]. Despite advances in acute management, effective strategies that selectively modulate secondary injury processes remain limited, highlighting the need to define actionable cellular and molecular regulators of the post-injury microenvironment [4, 5].

Resident microglia are central to this inflammatory response [6]. As the principal innate immune cells of the central nervous system (CNS), microglia rapidly sense injury-associated danger signals and undergo extensive transcriptional and functional remodeling [7, 8]. Rather than adopting binary phenotypes, injury-activated microglia exist along a dynamic spectrum of states that can either exacerbate secondary injury or facilitate repair processes, including debris clearance, trophic signaling and tissue remodeling [9]. Single-cell transcriptomic studies have further highlighted marked heterogeneity and plasticity of microglia responses after SCI [10-12]. However, the signaling nodes that govern state transitions, their temporal coordination, and their linkage to repair-relevant outcomes are still poorly understood [13]. This gap constrains the development of state-dependent immunomodulatory interventions.

Myeloid differentiation primary response 88 (MyD88) is a core adaptor of innate immune signaling [14, 15]. Downstream of most Toll-like receptors (TLRs), MyD88 transduces damage-associated molecular pattern (DAMP) cues to NF-κB pathways,

driving cytokine and chemokine production [16, 17]. Although our previous research demonstrated that global inhibition of MyD88 signaling could reduce neuroinflammation after CNS injury, such approaches lack cellular specificity and temporal precision, potentially suppressing protective immune functions while masking cell-specific mechanisms [18]. The microglia-intrinsic contribution of MyD88 across distinct phases of SCI has not been systematically examined. Furthermore, it is unclear whether manipulating MyD88 can actively redirect microglial state trajectories toward sustained repair-associated programs, rather than simply dampening inflammatory output.

In this study, we integrated bulk and single-cell transcriptomics with pharmacological inhibition, inducible microglia-specific genetic manipulation and translational nanomedicine engineering to suppress microglial MyD88 signaling after SCI. Our data showed that MyD88 signaling was rapidly induced and persistently engaged in microglia following injury and was associated with pro-inflammatory microglial programs and delayed recovery of homeostasis. Targeted MyD88 suppression reprogrammed microglia from an inflammatory to a migrating state and improved tissue preservation, reduced scarring, enhanced connectivity and promoted locomotor recovery. We further identified TGF-β signaling as required for the protective phenotype. Finally, we developed a microglia-targeted biomimetic nanoparticle platform to deliver the MyD88 inhibitor ST2825, which provided therapeutic benefits, establishing a proof-of-concept strategy for precision immunomodulation after SCI.

Materials and Methods

Animals

Adult female mice (8-10 w, 20-25 g) were obtained from the Experimental Animal Center of Air Force Medical University (Xi'an, China). To achieve microglia-specific deletion of *Myd88*, *Tmem119*^{CreERT2} mice (The Jackson Laboratory, stock no. 031820) were crossed with *Myd88*$^{fl/fl}$ mice (stock no. 009108), generating *Tmem119*^{CreERT2};*Myd88*$^{fl/fl}$ conditional knockout (cKO) mice [19]. *Myd88*$^{fl/fl}$ littermates served as wild-type (WT) controls. Animals were housed under specific pathogen-free conditions (12 h light/dark cycle) with ad libitum access to food and water. Investigators were blinded to genotype and treatment during data acquisition and quantification when feasible.

Tamoxifen-induced recombination

Tamoxifen (TAM; MedChemExpress, HY-13757A) was dissolved in corn oil and administered by oral gavage at 200 mg/kg once daily from day -11 to day -7 relative to SCI. SCI was performed 7 days after the final TAM administration. Microglia-restricted recombination was validated in uninjured spinal cord sections using immunofluorescence staining for TMEM119 and MyD88.

SCI model

A forceps-mediated spinal cord crush injury model was used [20]. Mice were anesthetized with isoflurane (1.5-2.5% in oxygen), placed on a heating pad, and subjected to laminectomy at the T9 vertebral level. A No. 5 Dumont forceps (Fine

Science Tools) fixed on a stereotaxic apparatus was applied to the exposed spinal cord for 5 s to induce a standardized crush injury. Sham-operated mice underwent laminectomy without forceps application. Postoperative care included buprenorphine for analgesia twice daily for 3 days and manual bladder expression twice daily until recovery.

Experimental design and tissue collection

For temporal profiling of MyD88 signaling, lesion-centered spinal cord tissue was collected at 9, 18, 36 and 72 h post-injury for immunoblotting, and at 3, 7, 14 and 28 days post-injury (dpi) for immunofluorescence analyses; for bulk RNA sequencing (RNA-seq) and single-cell RNA sequencing (scRNA-seq), a 1 cm spinal cord segment centered on the lesion epicenter (extending 0.5 cm rostral and 0.5 cm caudal) was collected at 3 dpi; for histological analyses, tissues were collected at 3 dpi (neuronal preservation) and 28 dpi (scar and axonal markers). Bidirectional axonal tracing was performed at 10-13 weeks post-injury. Sample sizes (n) for each experiment are detailed in the corresponding figure legends.

Exclusion criteria included perioperative death, incomplete injury, severe surgical complications, and marked body weight loss beyond predefined thresholds (≥20%).

***In vivo* pharmacological inhibition of MyD88 signaling (ST2825)**

ST2825 (MedChemExpress, HY-50937) was dissolved in PBS containing 0.1% DMSO and administered immediately after injury by bilateral intraspinal

microinjection into the lesion site at a total dose of 2.5 μg per mouse (1.25 μg/side in 0.5 μL; total injection volume 1.0 μL) according to an established dosing strategy [21, 22]. Injections were performed with a Hamilton syringe fitted with a glass micropipette at 50 nL/min (0.5 μL per site) at 0.3 mm lateral and 0.7 mm depth from the dorsal surface. Vehicle-injected mice served as controls.

TGF-β receptor blockade (LY2109761)

To test the requirement of TGF-β signaling, LY2109761 (MedChemExpress, HY-12075) was administered by oral gavage at 50 mg/kg twice daily for 3 consecutive days starting immediately after SCI [23]. Corn oil was used as the vehicle control. TGF-β pathway activity was assessed by immunofluorescence for nuclear phosphorylated SMAD3 (pSMAD3) at 3 dpi.

Cell culture experiments

The N9 murine microglial cell line was cultured in DMEM supplemented with 10% fetal bovine serum and 1% penicillin/streptomycin at 37 °C in 5% CO_2. Cells were pretreated with control peptide (CP) or MyD88 inhibitory peptide (MIP; Novus Biologicals, NBP2-29328) at 100 μM for 24 h, followed by stimulation with LPS (Sigma, L2630, 100 ng/mL) or IL-4 (MedChemExpress, HY-P70653, 40 ng/mL) for 24 h [24].

Primary microglia culture and ST2825 treatment

Primary microglia were prepared from P0-P1 neonatal mice as previously described with minor modifications. Briefly, cerebral cortices were dissociated with trypsin and

plated to generate mixed glial cultures. After 10 days, microglia were isolated by shaking and seeded on poly L-lysine-coated coverslips at 1×10^5 cells/cm². Cells were pretreated with ST2825 (5 μM) or vehicle for 12 h, followed by LPS stimulation (100 ng/mL) for 12 h. Supernatants were collected for multiplex ELISA, and cells were fixed for immunofluorescence staining.

Multiplex ELISA

TNF-α, IL-1β, IL-10, CSF-1, TGF-β1 and IGF-1 in culture supernatants were quantified with multiplex ELISA kits (Ruixin Biotech; RX202412M, RXW203063M, RX203075M, RXW200222M, RXW202402M, RXW202483M) according to the manufacturer's instructions. Concentrations were calculated from standard curves.

Immunofluorescence staining and image acquisition

Mice were perfused transcardially with PBS followed by 4% paraformaldehyde (PFA). Spinal cords were post-fixed in 4% PFA for 4 h, cryoprotected in 30% sucrose, embedded and sectioned longitudinally at 14 μm. Sections were permeabilized and blocked in 5% normal donkey serum containing 0.3% Triton X-100 and incubated with primary antibodies against MyD88, Iba1, F4/80, GFAP, iNOS, Arg-1, TMEM119, pSMAD3, NF200, GAP43, ChAT, TUJ1 and synaptophysin (Table S1). After incubation with fluorophore-conjugated secondary antibodies, nuclei were counterstained with DAPI.

Images were acquired with an Olympus FV3000 laser-scanning confocal microscope or an Olympus VS200 slide scanner under identical acquisition settings.

Quantification was done using ImageJ in predefined regions of interest (ROIs) spanning the lesional and peri-lesional regions. For high-magnification views, confocal Z-stacks were taken with a step size of 0.5-1 μm over a total depth of 5-10 μm. Maximum intensity projections were generated in Olympus FV31S-SW software for subsequent quantification.

Histology and scar quantification

For Nissl staining, sections were processed using cresyl violet and imaged using an Olympus VS200 microscope. For peri-lesional neuron quantification, three standardized ROIs (200 × 200 μm each) were randomly selected in the gray matter 300 μm rostral and caudal to the lesion border. Nissl-positive neurons were identified by the following criteria: cell diameter > 15 μm, presence of a clear nucleolus, and abundant cytoplasmic Nissl substance with a tigroid appearance. Data for each animal represent the mean of three ROIs. For hematoxylin and eosin (H-E) staining, sections followed standard protocols, and scar area was quantified at 28 dpi. Scar area was considered as the non-neural dense tissue region and cavitation within the lesion boundary, and ImageJ was used for quantification.

Western blotting

Lesion-containing spinal cord tissues were homogenized in RIPA buffer supplemented with protease and phosphatase inhibitors. Protein concentration was determined using a BCA assay. Equal amounts of protein were separated by SDS-PAGE, transferred to PVDF membranes and probed with antibodies against TLR4, MyD88, TNF-α, IL-1β, iNOS, Arg-1, GAP43 and β-actin (Table S1). Signals

were detected using enhanced chemiluminescence and quantified by densitometry (ImageJ). Target band intensity was normalized to β-actin.

Bulk RNA-seq and bioinformatics

For bulk RNA-seq, each sample was derived from one individual mouse, and no biological pooling was performed. Thus, each group included 5 independent biological samples (n = 5 mice per group). Sequencing was performed on an Illumina NovaSeq 6000 (PE150 mode) following cluster generation via the cBot system. After quality control (removal of adapters, low-quality reads and duplicates), clean reads were mapped to the mm10 reference genome using Hisat2. Gene abundances were normalized to TPM. Differential expression analysis was executed with limma (v3.52.1), applying thresholds of $p < 0.05$ and $|\log_2FC| > 0.575$. Functional annotation, including GO and GSEA, was performed using clusterProfiler (v4.9.3). Visualization was generated via GseaVis (v0.0.9) and ggplot2 (v3.3.6) [25, 26].

scRNA-seq and analyses

Single-cell suspensions were prepared from pooled spinal cord tissue (5 mice per sample) centered on the lesion epicenter at 3 dpi, and scRNA-seq libraries were constructed with the GEXSCOPE® Single-Cell RNA Library Kit (Singleron Biotechnologies) according to the manufacturer's instructions. Libraries were sequenced on the Illumina NovaSeq 6000 platform. Raw sequencing reads were processed through the Singleron analysis pipeline, including read alignment, cell barcode/UMI processing and generation of the gene–cell expression matrix. After removing doublets with DoubletFinder (v2.0.3), we retained high-quality cells with

300-10,000 features, < 20% mitochondrial genes, and < 0.1% hemoglobin genes. After UMAP clustering in Seurat (v4.4.0), cell identities were assigned with SingleR and canonical marker genes. Pseudotime trajectories were reconstructed by Monocle2 (v2.22.0). Gene set activity scoring relied on AUCell (v1.18.1) to quantify pathway signatures [27]. In addition, we used the Tabulae Paralytica single-cell atlas [28] to independently assess the expression of *Myd88* across major cell types after SCI.

Behavioral testing

Hindlimb locomotor function was assessed using the Basso Mouse Scale (BMS) [29] by two independent observers blinded to group allocation. CatWalk XT gait analysis (Noldus) [30] was performed at 28 dpi to quantify average speed, stride length, initial dual stance and terminal dual stance. Mice were acclimated to the apparatus for 3 days. Runs were included only if they met predefined criteria (uninterrupted run; speed variation < 60%).

Axonal tracing

Bidirectional tracing was performed at 10 weeks post-injury [31]. For anterograde tracing, rAAV9-hSyn-EGFP (2.00×10^{12} vg/mL; BrainCase) was injected cranially to the lesion at four sites (1 µL/site, 50 nL/min). For retrograde tracing, Fluoro-Gold (4% in H_2O; Santa Cruz, sc-358883) was injected caudally to the lesion (100 nL, 50 nL/min). Spinal cords were harvested at 10 weeks + 5 days (Fluoro-Gold) or 13 weeks (EGFP) post-injury as indicated. EGFP and Fluoro-Gold signals were quantified in standardized ROIs cranial and caudal to the lesion border.

Compound muscle action potential (CMAP) recording and analysis

CMAP recordings were performed at 10 weeks post-injury. Briefly, a bipolar stimulating electrode was placed on the exposed spinal cord cranial to the lesion site, and a recording electrode was inserted into the hindlimb gastrocnemius muscle. Latency was measured from the stimulus artifact onset to the first deflection of the CMAP waveform from baseline. Amplitude was measured as the peak-to-peak voltage. All recordings were conducted under constant body temperature (37 °C) with standardized electrode placement.

Biomimetic nanoparticle fabrication and characterization

MG1-modified fluorescent liposomes (vehicle)

SPC, cholesterol, DSPE-PEG-MG1 (MG1 sequence: CHHSSSARC, cyclized via Cys1-Cys9) and DiD (all from Shanghai Apeptide Co.,Ltd) were co-dissolved in 1 mL chloroform. Solvent was removed under reduced pressure to form a thin lipid film, which was hydrated with ultrapure water under sonication. The suspension was processed by bath sonication (180 W) and extruded using a mini-extruder (Avanti) through a 100-nm polycarbonate membrane (Whatman) to obtain MG1-modified fluorescent liposomes.

Microglia membrane-coated, MG1-modified, ST2825-loaded liposomes

SPC, cholesterol, DSPE-PEG-MG1, DiD and ST2825 were co-dissolved in 1 mL of chloroform and processed by thin-film hydration, bath sonication (180 W), and extrusion through 100-nm polycarbonate membranes to yield ST2825-loaded

MG1-modified liposomes.

Liposomes were then mixed with primary microglia membranes at a 1:1 mass ratio, sonicated in an ice bath for 30 s, and incubated at room temperature for 2 h to generate MG1-modified, microglia membrane-coated, DiD-labeled vehicles or ST2825-loaded nanoparticles (DSPE@MG or ST2825·DSPE@MG). Drug loading and encapsulation efficiency were 6.2% and 93.8%, respectively.

In vivo lesion retention and cellular uptake

For lesion targeting, DiD-labeled nanoparticles were administered locally after SCI. At 3 days after administration, spinal cords were harvested for *ex vivo* fluorescence imaging using an IVIS Spectrum system (PerkinElmer) and radiant efficiency profiling along the rostrocaudal axis. Spinal cord sections were immunostained with Iba1 to detect nanoparticle colocalization with microglia.

Statistical analysis

We conducted statistical analyses using R (v4.2.0) and GraphPad Prism (v8.0.2). All data are shown as mean ± SD. Normality was assessed with the Shapiro-Wilk test; appropriate data transformations or nonparametric tests were applied when necessary. Missing data were not imputed unless specified. For two-group comparisons, an unpaired two-tailed Student's *t*-test was used for normally distributed data, and the Wilcoxon rank-sum test was applied for non-normal data. For comparisons among multiple groups, one-way ANOVA or two-way repeated-measures ANOVA followed by Tukey's post hoc test was applied for normally distributed data; otherwise, the

Kruskal-Wallis test with Dunn's post hoc test was used for non-normally distributed data. We used Spearman's rank correlation for correlation analyses. $p < 0.05$ was considered statistically significant. All experiments included at least three biological replicates unless stated otherwise in the figure legends. All comparisons across multiple related readouts were viewed as exploratory analyses; accordingly, no formal correction for multiplicity was applied.

Results

Spatiotemporal activation of MyD88 signaling in microglia after SCI and association with microglial state markers

To examine the temporal dynamics of MyD88 signaling following SCI, we used a forceps-mediated crush injury model (Figure 1A). We reanalyzed our previously generated bulk RNA-seq dataset [32] by gene set enrichment analysis (GSEA) and found notable enrichment of NF-κB signaling downstream of MyD88 at 1, 3, 7 dpi (Figure 1B). Consistently, *Myd88* mRNA abundance at the lesion site increased across these time points relative to that in the sham controls (Figure 1C). At the protein level, immunoblotting demonstrated that TLR4 and MyD88 were upregulated as early as 9 h post-injury and remained elevated for 72 h, indicating rapid and sustained activation of the TLR-MyD88 axis during the acute phase (Figure 1D).

To localize *Myd88* expression across spinal cord cell types, we reanalyzed the Tabulae Paralytica SCI single-cell atlas [28]. Among 14 annotated populations, *Myd88* expression was highest in microglia and vascular endothelial cells (Figure 1E-F). Within microglia, AUCell-based pathway scoring indicated sustained activity

of the TLR-MyD88 gene program across the post-injury time course (uninjured to 2 months post-injury) (Figure 1G). This pointed to microglia as the primary spinal cell type exhibiting sustained MyD88-dependent signaling after SCI.

We next validated these observations in our SCI model by tracking immunofluorescence changes over time at 3, 7, 14 and 28 dpi. MyD88 immunoreactivity rose sharply at 3 and 7 dpi and predominantly colocalized with $Iba1^+$ microglia at the lesion site (Figure 1H). Quantification revealed that the density of $MyD88^+Iba1^+$ microglia peaked at 3 dpi and progressively declined thereafter (Figure 1I). In parallel, microglia exhibited robust activation early after injury and subsequently underwent morphological remodeling, including an increased soma area and higher protrusion numbers at later stages (Figure 1I). Finally, to relate *Myd88* expression to microglial state markers during the acute stage, we assessed correlations between *Myd88* and canonical marker genes at 1, 3, 7 dpi. *Myd88* did not correlate with the homeostatic marker *P2ry12* but showed significant positive correlations with *Nfkb1*, *Nos2*, *Arg1* and *Tgfb1* (all $p < 0.01$) (Figure 1J), indicating that elevated *Myd88* is associated with activated microglial state remodeling rather than with baseline homeostasis.

MyD88 inhibition induces phenotypic and secretory reprogramming of microglia *in vitro* and *in vivo*

To ask whether suppression of MyD88 signaling can shift microglial response programs, we began with the N9 microglial cell line. We pretreated cells with a control peptide (CP) or a MyD88 inhibitory peptide (MIP; Novus Biologicals,

NBP2-29328) and then stimulated them with LPS or IL-4 to bias pro-inflammatory or repair-associated programs, respectively. MIP pretreatment reduced LPS-induced iNOS immunoreactivity compared to CP-treated controls (Figure S1A). Additionally, Arg-1^{+} cells were detected under MIP-treated conditions (MIP-CON and MIP-LPS) and displayed a more ramified morphology resembling that of the IL-4-positive control (Figure S1A-B), indicating that blocking MyD88 reduces LPS-induced inflammation while promoting repair *in vitro*.

We next validated these findings in primary microglia with a different MyD88 inhibitor, ST2825 (Figure 2A). CCK-8 assays confirmed that ST2825 at 5 μM for 12 h did not cause significant microglial cytotoxicity or apoptosis (Figure S1C-D). In vehicle-treated cultures, LPS induced amoeboid morphology and robust iNOS expression (CON-LPS; Figure 2C-D). By contrast, ST2825 pretreatment reduced iNOS signal and increased Arg-1 immunoreactivity in LPS-stimulated microglia (ST2825-LPS; Figure 2C-D). Consistent with this, ST2825-treated microglia exhibited smaller somata with elongated bipolar processes, generating rod-like morphologies (Figure 2C). To assess functional output, cytokines and growth factors in the culture supernatants were measured by multiplex ELISA. ST2825 markedly reduced LPS-induced TNF-α and IL-1β levels, whereas IL-10, CSF-1, IGF-1 and TGF-β1 levels were preserved compared to those in the vehicle-LPS controls (Figure 2E). CSF-1, TGF-β1 and IGF-1 were detectable at relatively high levels under resting conditions (CON-CON and ST2825-CON) (Figure 2E). These data suggest that MyD88 inhibition dampens pro-inflammatory outputs while maintaining

repair-associated secretions in primary microglia.

We then explored whether ST2825 modulated microglia responses *in vivo* after SCI (Figure 2B). ST2825 was bilaterally injected into the lesion site immediately after injury. At 3 dpi, MyD88 immunoreactivity at and around the lesion epicenter was reduced in ST2825-treated mice compared to that in vehicle controls (Figure 2F-G), accompanied by fewer F4/80^{+} cells and a reduced density of MyD88^{+} microglia within the lesion (Figure 2G). In the same regions, GFAP signal intensity did not differ between groups (Figure 2F-G), suggesting preferential effects on microglia at an early time point. At 7 dpi, vehicle-treated mice showed abundant iNOS^{+} microglia in peri-lesional areas, whereas ST2825 reduced iNOS^{+} microglia and increased Arg-1^{+} microglia (Figure 2H-I), consistent with an *in vivo* shift in marker profiles. To evaluate the tissue-level consequences, we performed Nissl staining. At 3 dpi, ST2825-treated mice exhibited higher densities of Nissl body-positive neurons in peri-lesional regions (Figure 2J-K). At 28 dpi, scar area was reduced in the ST2825 group, although tissue cavitation at the injury epicenter remained evident (Figure 2J-K). Collectively, these findings link acute MyD88 inhibition to microglial reprogramming and neuronal preservation, with sustained effects on tissue remodeling.

Microglia-specific MyD88 deletion attenuates neuroinflammation and accelerates recovery of homeostasis after SCI

To define the microglia-intrinsic contribution of MyD88 to SCI pathology, we generated inducible microglia-specific MyD88 conditional knockout mice by crossing

Tmem119^{CreERT2} mice with *Myd88*$^{fl/fl}$ mice (Figure 3A). After tamoxifen induction, MyD88 loss was restricted to TMEM119^{+} microglia, with *Myd88*$^{fl/fl}$ littermates serving as WT controls (Figure 3C, Figure S2A-C). We analyzed spinal cord transcriptomes at 3 dpi under sham and SCI conditions (Figure 3B). Bulk RNA-seq revealed a clear separation between WT-SCI and cKO-SCI samples (Figure S3A), and identified 36 upregulated and 102 downregulated differentially expressed genes (DEGs) in cKO-SCI relative to WT-SCI spinal cords (Figure 3D). Functional enrichment analysis showed that genes upregulated in cKO-SCI were linked to axon regeneration and neural repair, whereas downregulated genes mapped to microglia activation, neuroinflammatory responses, and TLR signaling (Figure 3E; Figure S3B). GSEA further showed suppression of NF-κB signaling and relative enrichment of neurogenesis in cKO-SCI tissue (Figure 3F; Figure S3C).

We next used scRNA-seq to characterize cellular composition and microglial programs at single cell resolution across four groups (WT-Sham, WT-SCI, cKO-Sham, cKO-SCI), which produced 38,919 cells and 12 major cell types after quality control and clustering (Figure 3G; Figure S3D) [12]. Relative to WT-SCI, the microglial proportion dropped by ~2.4% in cKO-SCI (Figure 3G). Quantitative analysis showed that the average *Myd88* expression level in cKO-SCI microglia was reduced by 70.98% compared with WT-SCI (0.0398 vs. 0.1370 normalized UMI), while expression in all other cell types remained unchanged between groups (Figure 3H-I; Figure S3E). UMAP feature plots and violin plots of apoptosis score in microglia revealed no significant difference between cKO-SCI and WT-SCI groups

409 (Figure S3F), ruling out the possibility that the observed state shift was driven by
410 selective cell death.

411 We next validated these molecular changes at the tissue level at 3 dpi.
412 Immunofluorescence showed reduced MyD88 signal within and around the lesion
413 epicenter in cKO-SCI mice compared with WT-SCI controls (Figure 3J),
414 accompanied by fewer $MyD88^{+}F4/80^{+}$ cells and reduced $F4/80^{+}$ cell density in the
415 lesion region (Figure 3K). In microglia, pathway-level analyses further supported
416 attenuation of inflammatory response and immune activation programs in cKO-SCI,
417 including reduced enrichment of leukocyte activation-related gene sets (Figure 3L-M;
418 Figure S3G). Consistent with transcriptomic findings, immunoblotting at 3 dpi
419 showed lower TNF-α and IL-1β protein levels in cKO-SCI spinal cords (Figure 3N).

420 Finally, we examined microglia activation markers at the lesion site. Compared
421 with WT-SCI, cKO-SCI spinal cords exhibited reduced iNOS immunoreactivity and
422 increased Arg-1 fluorescence intensity, with a higher number of $Arg\text{-}1^{+}$ microglia in
423 the lesion region (Figure 3O). Immunoblotting corroborated reduced iNOS protein
424 levels in cKO-SCI, while Arg-1 protein levels were comparable between groups
425 (Figure 3P). In addition, $TMEM119^{+}$ homeostatic microglia reappeared earlier in the
426 lesion area of cKO mice than in that of WT mice (Figure S4A-B). Together, these
427 data demonstrate that microglial MyD88 deletion suppresses acute inflammatory
428 signaling and accelerates recovery of homeostatic microglial features after SCI.

429 **Microglia-specific MyD88 deletion shifts microglial states toward a migrating**
430 **program and is associated with improved repair and functional recovery**

Given the dynamic state transitions of microglia after SCI, we investigated whether microglial MyD88 deletion reshapes the microglial state composition and is related to repair outcomes (Figure 4A). Based on published cell-state annotations [12], microglia were classified into three transcriptional states: homeostatic (*P2ry12*, *Siglech*), migrating (*Spp1*, *Igf1*), and inflammatory (*Cd63*, *Lyz2*) (Figure 4B; Figure S5A). Functional enrichment analysis indicated that homeostatic microglia were enriched for tissue homeostasis and remodeling terms, migrating microglia for cell migration and axonogenesis, and inflammatory microglia for inflammatory activation and apoptosis-associated responses (Figure 4C).

In the acute phase, cKO-SCI spinal cords exhibited a modestly increased proportion of migrating microglia and a reduced proportion of inflammatory microglia compared with WT-SCI (Figure 4D). The cell numbers and proportions for each subpopulation across groups are summarized in Table S2. We used pseudotime trajectory analysis to model state transitions. Microglia were arranged along a continuum from homeostatic to injury-associated states, progressing through a migrating intermediate toward an inflammatory endpoint (Figure 4E-F). Of note, cKO-SCI microglia were redistributed along this trajectory, with reduced representation at the inflammatory end and increased representation toward the migrating segment (Figure 4G). We next asked whether the observed shift in microglial states was functionally significant by performing ligand-receptor interaction analysis. This analysis showed stronger intercellular communication between the migrating and inflammatory subpopulations, as well as between

453 migrating microglia and neurons, in cKO-SCI compared with WT-SCI (Figure 4H),
454 indicating that the proportional redistribution is sufficient to produce biologically
455 meaningful changes in microglial crosstalk.

456 We next assessed whether this state shift was accompanied by improved tissue
457 repair. Immunofluorescence analyses at 14 and 28 dpi showed a higher $TMEM119^{+}$
458 signal in peri-lesional regions in cKO-SCI than in WT-SCI at both time points (Figure
459 S5B-C), consistent with sustained recovery of homeostatic features. At 28 dpi,
460 peri-lesional gray matter in cKO-SCI mice displayed a stronger NF200 signal,
461 increased GAP43 immunoreactivity near the lesion border, and better-preserved
462 neuronal morphology (Figure 4I-J). In the ventral horn, cKO-SCI mice exhibited a
463 higher number of $ChAT^{+}NF200^{+}$ motor neurons (Figure 4K-L). TUJ1/synaptophysin
464 staining further showed increased neuronal and synaptic puncta density around the
465 lesion (Figure S5C). In parallel, the scar area at 28 dpi was reduced in cKO-SCI
466 relative to WT-SCI (Figure 4J; Figure S5D), and immunoblotting confirmed increased
467 GAP43 protein abundance (Figure 4M). Fibronectin (encoded by *Fn1*), an
468 extracellular matrix protein implicated in tissue repair and axonal guidance, revealed
469 sustained perilesional expression in cKO-SCI microglia compared with WT-SCI
470 (Figure S6A-B). Functionally, cKO-SCI mice exhibited improved hindlimb locomotor
471 recovery by BMS scoring (Figure 4N) and superior gait parameters by CatWalk
472 analysis at 28 dpi (Figure 4O-P). Finally, bidirectional tracing at 10 weeks post-injury
473 showed increased Fluoro-Gold labeling cranial to the lesion and enhanced
474 rAAV9-hSyn-EGFP signal caudal to the lesion in cKO-SCI mice (Figure 4Q-R;

Figure S5E), indicating enhanced long-range axonal connectivity. Consistent with this, CMAP recordings at the same time point revealed significantly improved amplitude and reduced latency in cKO-SCI mice compared with WT-SCI controls (Figure S7), providing functional evidence for improved axonal conductivity across the lesion site.

TGF-β signaling is required for the protective phenotype associated with microglial MyD88 deletion

In search of candidate mediators downstream of microglial MyD88 deletion, we examined gene dynamics along the microglial pseudotime trajectories. *Myd88* expression remained reduced in cKO-SCI microglia throughout pseudotime, including late pseudotime corresponding to inflammatory states (Figure 5A). In parallel, *Tnf* exhibited a late pseudotime peak in WT-SCI microglia that was blunted in cKO-SCI microglia (Figure 5A). By comparison, *Tgfb1* displayed higher expression in cKO-SCI microglia across pseudotime (Figure 5A), pointing to enhanced TGF-β signaling as a candidate pathway associated with the state shift. CellChat analysis showed stronger reparative signaling (FGF, TGF-β) and weaker pro-inflammatory signaling (EGF, OSM, TNF) in cKO-SCI compared with WT-SCI (Figure 5B), and the prominent TGF-β upregulation aligned with increased *Tgfb1* expression along the microglial pseudotime trajectory. We next analyzed the expression profiles of *Tgfb1* and its receptors (*Tgfbr1*, *Tgfbr2*, *Acvr1*) across major cell types to clarify the cellular source and targets of TGF-β signaling. *Tgfb1*, *Tgfbr1* and *Tgfbr2* were predominantly expressed by microglia, whereas *Acvr1* was expressed in both neurons and microglia. Astrocytes showed negligible expression of TGF-β signaling components in our

497 dataset (Figure S8A). Within the microglial compartment, homeostatic and migrating
498 microglia exhibited higher expression of *Tgfb1*, *Tgfbr1* and *Tgfbr2* than inflammatory
499 microglia, implying that at 3 dpi, microglia serve as both the principal source and the
500 primary target of TGF-β1.

501 We then tested the functional relevance of TGF-β signaling by administering the
502 TGF-β receptor inhibitor LY2109761 to cKO mice immediately after SCI for 3
503 consecutive days (Figure S8B). We used nuclear pSMAD3 as a downstream readout
504 of TGF-β signaling at 3 dpi (Figure 5C) [33]. Compared with WT-SCI, the absolute
505 number of pSMAD3$^+$F4/80$^+$ cells was reduced in cKO-SCI spinal cords; however, the
506 fraction of pSMAD3$^+$ cells within the F4/80$^+$ population did not differ between groups
507 (Figure 5D). Meanwhile, cKO-SCI tissue exhibited an increased nuclear pSMAD3
508 signal in peri-lesional non-microglia (Figure 5C). Importantly, LY2109761 markedly
509 reduced pSMAD3 signal (Figure 5C-D), and increased the density of F4/80$^+$ cells
510 with a more activated morphology (Figure 5C-D), indicating the failure of the
511 anti-activation mechanism of microglia in cKO mice without TGF-β signaling
512 intervention. Ligand-receptor analysis further confirmed *Tgfb1*-*Tgfbr1*/*Tgfbr2* as the
513 dominant signaling axis, with *Acvr1* contributing weakly (Figure S8C). Together with
514 the predominant microglial expression of *Tgfbr1*/*Tgfbr2* (Figure S8A) and the active
515 inter-subpopulation crosstalk observed after SCI (Figure 4H), these data establish a
516 TGF-β autocrine loop as the primary mechanism by which MyD88-deficient
517 microglia regulate their reprogrammed state.

518 To ask whether TGF-β signaling contributes to tissue preservation and functional

519 recovery in cKO mice, we performed Nissl staining and behavioral tests. Peri-lesional
520 neuronal morphology was better preserved in cKO-SCI mice than WT-SCI at 3 and 28
521 dpi, whereas LY2109761-treated cKO-SCI mice showed pronounced neuronal loss
522 and tissue disruption (Figure 5E). In agreement with these histological changes,
523 LY2109761 abolished locomotor improvement in cKO-SCI mice as measured by
524 longitudinal BMS scoring and CatWalk analysis (Figure 5F-G). These results indicate
525 that intact TGF-β signaling is required for the tissue-protective and functional benefits
526 associated with microglial MyD88 deletion (Figure 5H).

527 **Microglia-targeted biomimetic nanoparticles enable lesion-retained delivery of**
528 **ST2825 and improve recovery after SCI**

529 To enhance the delivery of ST2825 to the injured spinal cord and promote microglia
530 uptake, we developed microglia membrane-coated, MG1 peptide-modified
531 biomimetic nanoparticles (ST2825·DSPE@MG) (Figure 6A) [34]. Dynamic light
532 scattering (DLS) showed that DSPE@MG and ST2825·DSPE@MG had comparable
533 hydrodynamic diameters (~90-140 nm) with low polydispersity (PDI < 0.2) and
534 mildly negative zeta potentials (~-15 to -30 mV), indicating stable and monodisperse
535 formulations (Figure 6B). Transmission electron microscopy (TEM) revealed
536 spherical particles with a core-shell morphology consistent with membrane coating
537 (Figure 6C). *In vitro* drug release assays demonstrated that ST2825·DSPE@MG
538 exhibited sustained release of ST2825 over 72 h and achieved ~70% cumulative
539 release (Figure S9A). Colloidal stability tests confirmed that particle size, PDI and
540 zeta potentials remained stable at 4 ℃ over 14 days (Figure S9A). Size distribution by

intensity confirmed a unimodal distribution for both DSPE@MG and ST2825·DSPE@MG, and no appreciable peak shift or broadening after drug loading (Figure S9B).

We next assessed lesion targeting using DiD-labeled nanoparticles following local administration. *Ex vivo* fluorescence imaging at 3 dpi showed strong DiD signals concentrated at the injury epicenter in both DSPE@MG and ST2825·DSPE@MG groups (Figure 6D). Radiant efficiency profiles along the rostrocaudal axis peaked at the lesion segment and declined into peri-lesional regions (Figure 6D). *In vivo* fluorescence imaging from 1 to 7 days post-administration further confirmed that the DiD-labeled nanoparticle signal remained strictly confined to the lesion segment without detectable leakage to adjacent segments or systemic distribution (Figure S9C). Imaging revealed extensive colocalization of DiD-labeled nanoparticles with $Iba1^+$ microglia at the lesion boundary, with a punctate intracellular DiD signal (Figure 6E). Quantitative analysis showed that ~65% of $Iba1^+$ microglia in the lesion area were DiD^+, with nearly all detectable DiD signal colocalizing with Iba1 (Figure S9D), demonstrating efficient and selective microglial uptake of the nanoparticles. We also prepared and characterized plain liposomes loaded with ST2825 as an additional control. They exhibited a uniform size distribution, good colloidal stability, high drug loading capacity (6.25%) and encapsulation efficiency (93.75%), and spherical morphology under TEM (Figure S9E-F). However, these plain liposomes did not produce a noticeable behavioral improvement (Figure S9G).

We then investigated whether microglia-targeted delivery of ST2825 modulates

563 early neuroinflammatory responses after SCI. At 3 dpi, ST2825·DSPE@MG
564 treatment reduced the number of F4/80^{+} cells and decreased iNOS signal within the
565 lesion region compared with DSPE@MG controls (Figure 6F-G). At the same time,
566 Arg-1 signal and the number of Arg-1^{+}Iba1^{+} cells were increased in the
567 ST2825·DSPE@MG group (Figure 6F-G), reflecting a shift in marker expression
568 patterns within the lesion microenvironment.

569 Lastly, we evaluated tissue remodeling and functional recovery. BMS scoring
570 showed improved locomotor performance in ST2825·DSPE@MG-treated mice
571 compared with DSPE@MG controls (Figure 6H), and CatWalk analysis at 28 dpi
572 further confirmed an improved gait performance (Figure 6I). H-E staining at 28 dpi
573 demonstrated a reduced scar area in the ST2825·DSPE@MG group (Figure 6J).
574 Together, these data indicate that biomimetic nanoparticle delivery of ST2825
575 enhances microglia uptake and improves functional recovery after SCI. Similar to the
576 findings in females, ST2825·DSPE@MG treatment in males promoted the transition
577 of lesion-associated microglia from a pro-inflammatory toward a repair-associated
578 phenotype (Figure S10A-B).

579 **Discussion**

580 SCI elicits a rapid and sustained innate immune response that drives secondary tissue
581 damage and constrains functional recovery [35]. MyD88 integrates signals from TLRs
582 and acts as a proximal adaptor for NF-κB-dependent inflammatory transcription.
583 Previous studies have demonstrated that global inhibition of MyD88 signaling can
584 attenuate inflammation following CNS injury [36, 37]. However, such

broad-spectrum interventions have key limitations: they mask the cell-type-specific functions of MyD88 and fail to actively drive injury-activated microglia toward a reparative state. The incremental contributions of the present study are threefold: (1) microglia-specific MyD88 conditional knockout was achieved for the first time in the context of SCI, revealing that microglia-intrinsic MyD88 signaling governs pathological state transitions; (2) TGF-β signaling was identified as a functional downstream bridge linking MyD88 suppression to tissue repair; and (3) a biomimetic nanodelivery strategy was developed based on this mechanistic understanding. Collectively, this work represents a paradigm shift from broad-spectrum anti-inflammatory intervention to precision microglial reprogramming.

A key finding of this study is that MyD88 signaling is activated shortly after SCI and remains elevated throughout the acute-to-subacute phase. Bulk transcriptomics and immunoblotting indicated sustained activation of the TLRs-MyD88 axis from hours to days after injury. Interrogation of the Tabulae Paralytica single-cell atlas further localized high *Myd88* expression to microglia, indicating that MyD88 induction after SCI was not uniformly distributed across spinal cord cell types. This temporal and cellular resolution has translational relevance, as the clinical failure of anti-inflammatory strategies in SCI has been attributed, in part, to imprecise treatment windows and inadequate cellular specificity, which can suppress beneficial immune functions while failing to target dominant pathological drivers [38-41]. Consistent with prolonged innate immune activation in chronic SCI [42], AUCell scoring suggested persistent TLRs-MyD88 pathway activity in microglia over weeks.

607 Endothelial enrichment of *Myd88* suggested potential vascular contributions.
608 Nevertheless, our microglia-specific genetic studies indicated that microglial MyD88
609 was a dominant determinant of pathological outcomes, aligning with emerging
610 evidence that microglia actively regulate lesion microenvironments and scar dynamics
611 rather than serving as passive responders [43-45].

612 The second major finding is that MyD88 activity is coupled with microglial state
613 remodeling after SCI. Across datasets, *Myd88* expression showed a weak association
614 with homeostatic markers but aligned with inflammatory and repair-associated marker
615 sets, suggesting that MyD88 engagement accompanied state transitions rather than
616 resting homeostasis. *In vitro*, two independent inhibitory approaches (MIP in N9 cells
617 and ST2825 in primary microglia) converged on a consistent phenotype: reduced
618 LPS-induced iNOS expression and decreased pro-inflammatory cytokine release
619 (TNF-α, IL-1β), with preservation of trophic mediators (IL-10, CSF-1, IGF-1,
620 TGF-β1). These findings support the concept that MyD88 inhibition does not simply
621 silence microglial activity but actively reprograms it toward a less damaging,
622 potentially pro-repair state. *In vivo*, local ST2825 administration confirmed these
623 features during the acute phase, including reduced $iNOS^{+}$ microglia, increased Arg-1
624 labeling, and improved perilesional neuronal preservation. Importantly, early
625 immunomodulation can have opposing consequences depending on timing and
626 cellular specificity: some components of the glial response, including aspects of scar
627 formation, can stabilize injured tissue and limit lesion spread [46, 47]. Our results
628 therefore support a microglia-targeted framework in which dampening maladaptive

signaling while preserving protective functions may be more effective than indiscriminate immunosuppression.

Using *Tmem119*^{CreERT2};*Myd88*$^{fl/fl}$ mice, we tested microglia-intrinsic MyD88 function while reducing confounding from peripherally derived myeloid cells. Although TMEM119 expression can be downregulated after SCI, this concern was mitigated by completing tamoxifen induction prior to injury with a 7-day washout period. This design ensured that CreERT2-mediated recombination primarily targeted homeostatic microglia before injury onset. Our scRNA-seq data confirmed that *Myd88* downregulation was strictly confined to microglia across all 12 major cell types analyzed. At 3 dpi, bulk RNA-seq demonstrated that microglial MyD88 deletion shifted the injured spinal cord transcriptome away from innate immune activation and toward axon growth and repair-associated programs. scRNA-seq further confirmed efficient *Myd88* reduction in microglia and revealed attenuation of inflammatory response and immune activation gene sets, including reduced enrichment of lymphocyte activation-related programs. These results suggest that microglial MyD88 contributes not only to intrinsic inflammatory amplification but also to broader immune network activation within the lesion environment. Tissue-level validation corroborated these transcriptomic findings, including reduced MyD88/F4/80 co-labeling and lower TNF-α and IL-1β protein levels. Together, these data position microglial MyD88 upstream of early inflammatory amplification that likely contributes to secondary injury cascades. They further support a model in which MyD88 signaling delays resolution by sustaining injury-associated inflammatory

programs, consistent with its established role in TLR signaling and NF-κB activation. Importantly, our state-based and trajectory-based analyses provide a framework that aligns with contemporary single-cell literature, which emphasizes microglial continua rather than binary “M1/M2” endpoints.

Beyond molecular signatures, our study links microglial MyD88 deletion to structural and functional outcomes. By classifying microglia into homeostatic, migrating and inflammatory states, we observed that cKO mice showed a reduced fraction of inflammatory microglia and an increased fraction of migrating microglia during the acute phase. Pseudotime analysis supported a continuum from homeostatic states through a migrating intermediate toward inflammatory endpoints, and MyD88 deletion redistributed cells away from inflammatory termini. This state redistribution was accompanied by a reduced scar area, enhanced GAP43 expression, improved preservation of neuronal markers, and increased synaptic puncta around the lesion. Functionally, these anatomical correlations translated into improved BMS scores and CatWalk gait parameters. Notably, bidirectional tracing and CMAP electrophysiology provided convergent anatomical and functional evidence for enhanced axonal connectivity across the lesion, a stringent and clinically relevant endpoint [48-50]. While astrocytes and fibroblasts are canonical drivers of scar formation, microglia modulate scar architecture and extracellular matrix dynamics through cytokine signaling, phagocytic clearance, and crosstalk with astrocytes and infiltrating immune cells [51-53]. Our data identify MyD88 as a microglial node linking innate immune signaling to tissue-scale remodeling after SCI.

A central mechanistic insight is that the protective phenotype associated with microglial MyD88 deletion requires intact TGF-β signaling. Along the microglial pseudotime trajectory, cKO microglia exhibited elevated *Tgfb1* expression and attenuated *Tnf* induction relative to WT, indicating a shift toward a TGF-β-permissive signaling environment. CellChat analysis confirmed a shift from pro-inflammatory to reparative intercellular signaling networks in cKO-SCI mice, further supporting the central role of TGF-β signaling in the protective phenotype. Pharmacological TGF-β receptor blockade with LY2109761 suppressed pSMAD3 expression and reversed tissue preservation and locomotor benefits in cKO mice, establishing pathway necessity. Notably, rather than passively dampening inflammation, MyD88-deficient microglia appear to actively rewire their signaling from pro-inflammatory outputs to autocrine TGF-β homeostatic reinforcement. This self-sustaining mechanism may explain the durability of the reprogrammed state, as the autocrine feedback loop could maintain microglial homeostasis beyond the initial injury phase. The enhanced crosstalk between migrating microglia and neurons further suggests that TGF-β signaling facilitates neuron-microglia communication, contributing to a pro-regenerative microenvironment. Although the absolute number of $pSMAD3^{+}$ microglia decreased in cKO tissue, nuclear pSMAD3 signal was increased in perilesional non-microglia, suggesting that microglial MyD88 deletion reshapes the inflammatory microenvironment and redistributes SMAD3 activation across cell types. These findings align with previous reports implicating TGF-β signaling in limiting inflammation, promoting resolution, and supporting CNS repair, including the

maintenance of microglial identity [33, 54-57].

To translate mechanistic insights into a therapeutically actionable modality, we engineered a microglia-targeted biomimetic nanoparticle platform (ST2825·DSPE@MG) that enhanced lesion-localized delivery and microglia uptake of ST2825. This delivery strategy strengthened modulation of microglia activation markers, improved tissue preservation, and enhanced locomotor recovery compared with control nanoparticles. Biomimetic membrane coating and peptide-mediated targeting have emerged as complementary strategies to improve cellular specificity and retention in complex injury microenvironments [34]. By integrating these principles for microglia-oriented delivery, our platform shows that microglia-targeted MyD88 modulation can be packaged into a translationally relevant strategy for SCI.

Several limitations should be acknowledged. First, the crush injury model does not permit absolute discrimination between spared and regenerated axons; future studies employing complete transection models and fluorescence-based labeling strategies will be required for rigorous distinction. Second, the majority of experiments were conducted on female mice. Although ancillary experiments confirmed that the core pharmacodynamic effects of ST2825·DSPE@MG are similar in males, dedicated studies with larger male cohorts are warranted. Third, it should be noted that the present study adopted DSPE@MG as the core control to address the primary proof-of-concept question of whether therapeutic efficacy is attributable to MyD88 inhibition. Comprehensive *in vivo* tissue distribution analysis, complete PK/PD evaluation, and immunogenicity assessment will be essential components of

subsequent preclinical development. Fourth, rigorous validation of the nanoparticle targeting advantage will require stepwise dissection of the respective contributions of the membrane coating and the MG1 peptide. Fifth, while our data support a model in which autocrine TGF-β signaling plays the dominant role in the protective phenotype, cell-type-specific TGF-β receptor knockout tools will be needed to precisely dissect autocrine versus paracrine contributions. Sixth, the scRNA-seq dataset lacked biological replicates for each condition; therefore, differences in cell-type proportions should be interpreted cautiously. Finally, we note that F4/80 labels both activated resident microglia and infiltrating macrophages in the injured spinal cord; accordingly, $F4/80^+$ cells are more accurately interpreted as "$F4/80^+$ myeloid cells" throughout this study; and the "migrating microglia" designation reflects transcriptomic classification rather than a direct inference of *in vivo* motility.

Conclusions

This study identifies microglial MyD88 as an early and persistent regulator of injury-activated microglia remodeling following SCI. Microglia-specific MyD88 deletion rebalances microglial state trajectories toward repair-associated programs, accompanied by reduced neuroinflammation, accelerated recovery of homeostasis, reduced scarring, enhanced axonal connectivity, and improved locomotor function. Mechanistically, these benefits require intact TGF-β signaling. Finally, microglia-targeted biomimetic nanoparticles enable localized MyD88 inhibition with therapeutic benefits, providing a translational route to leverage state-based immunomodulation in SCI.

List of abbreviations

SCI: Spinal cord injury; MyD88: Myeloid differentiation primary response 88; TLR: Toll-like receptor; NF-κB: Nuclear factor kappa-light-chain-enhancer of activated B cells; TGF-β: Transforming growth factor beta; cKO: Conditional knockout; WT: Wild-type; BMS: Basso Mouse Scale; ROIs: regions of interest; PK/PD: pharmacokinetic/pharmacodynamic; GAP43: Growth-associated protein 43; Iba1: Ionized calcium-binding adapter molecule 1; iNOS: Inducible nitric oxide synthase; Arg-1: Arginase-1; DSPE: 1,2-Distearoyl-sn-glycero-3-phosphoethanolamine; CMAP: compound muscle action potential; DEG: Differentially expressed gene; DLS: Dynamic light scattering; GSEA: Gene set enrichment analysis; scRNA-seq: Single-cell RNA sequencing; UMAP: Uniform manifold approximation and projection.

Ethics approval

All animal procedures were reviewed and approved by the Laboratory Animals Ethics Committee of the Air Force Medical University (Approval No. 20250224) and were conducted in accordance with the NIH Guide for the Care and Use of Laboratory Animals (NIH Publications No. 80-23, revised 1996).

Availability of data and materials

The datasets supporting the conclusions of this article are included within the article and its additional files (Figs. S1-S10, Table S1-S2).

Competing interests

The authors declare no conflict of interest.

Acknowledgements

AI tools were not used in this manuscript.

Funding

This work was supported by National Key Research and Development Program of China (No. 2024YFA1802502), National Natural Science Foundation of China (No. 82301552, 82271501, 82525039 and 82372404).

Author contributions

J.H., F.K., and Jintao Liu conceptualized and designed the study. Jintao Liu, B.Y., W.C., Jilu Liu, Y.G., H.M., X.G., L.G., S.L., Q.H., and M.Q. provided technical, methodological, material support, and resources. Jintao Liu, B.Y., W.C., Jilu Liu, and Y.G. contributed to the acquisition of data. Jintao Liu, B.Y., W.C., and Jilu Liu analyzed and interpreted the results. Jintao Liu, B.Y., W.C., Jilu Liu, Y.G., H.M., X.G., L.G., S.L., Q.H., and M.Q. provided formal analysis of the data and data curation. Jintao Liu, B.Y., W.C., and Jilu Liu prepared the first manuscript. J.H. and F.K. revised and edited the manuscript.

References

[1] Ahuja CS, Wilson JR, Nori S, Kotter MRN, Druschel C, Curt A, et al. Traumatic spinal cord injury. Nat Rev Dis Primers. 2017; 3: 17018.

[2] O'Shea TM, Burda JE, Sofroniew MV. Cell biology of spinal cord injury and repair. J Clin Invest. 2017; 127: 3259-70.

781 [3] Hellenbrand DJ, Quinn CM, Piper ZJ, Morehouse CN, Fixel JA, Hanna AS.
782 Inflammation after spinal cord injury: a review of the critical timeline of signaling
783 cues and cellular infiltration. J Neuroinflammation. 2021; 18: 284.

784 [4] Sofroniew MV. Dissecting spinal cord regeneration. Nature. 2018; 557: 343-50.

785 [5] Fan H, Tang HB, Chen Z, Wang HQ, Zhang L, Jiang Y, et al. Inhibiting
786 HMGB1-RAGE axis prevents pro-inflammatory macrophages/microglia polarization
787 and affords neuroprotection after spinal cord injury. J Neuroinflammation. 2020; 17:
788 295.

789 [6] Prinz M, Priller J. Microglia and brain macrophages in the molecular age: from
790 origin to neuropsychiatric disease. Nat Rev Neurosci. 2014; 15: 300-12.

791 [7] Zhao J, Sheng X, Ding Y, Wen H, Zheng L, Sun Y, et al. KDM6A/MMP-3
792 epigenetic axis governs macrophage senescence after spinal cord injury for mediating
793 the regenerative niche to promote neurological repair. J Adv Res. 2025.

794 [8] Wu W, He Y, Chen Y, Fu Y, He S, Liu K, et al. In vivo imaging in mouse spinal
795 cord reveals that microglia prevent degeneration of injured axons. Nat Commun. 2024;
796 15: 8837.

797 [9] Ransohoff RM. A polarizing question: do M1 and M2 microglia exist? Nat
798 Neurosci. 2016; 19: 987-91.

799 [10] Masuda T, Sankowski R, Staszewski O, Prinz M. Microglia heterogeneity in the
800 single-cell era. Cell Rep. 2020; 30: 1271-81.

801 [11] Hammond TR, Dufort C, Dissing-Olesen L, Giera S, Young A, Wysoker A, et al.

802 Single-cell RNA sequencing of microglia throughout the mouse lifespan and in the
803 injured brain reveals complex cell-state changes. Immunity. 2019; 50: 253-71.e6.

804 [12] Milich LM, Choi JS, Ryan C, Cerqueira SR, Benavides S, Yahn SL, et al.
805 Single-cell analysis of the cellular heterogeneity and interactions in the injured mouse
806 spinal cord. J Exp Med. 2021; 218: e20210040.

807 [13] Keren-Shaul H, Spinrad A, Weiner A, Matcovitch-Natan O, Dvir-Szternfeld R,
808 Ulland TK, et al. A unique microglia type associated with restricting development of
809 Alzheimer's disease. Cell. 2017; 169: 1276-90.e17.

810 [14] Kawai T, Akira S. The role of pattern-recognition receptors in innate immunity:
811 update on Toll-like receptors. Nat Immunol. 2010; 11: 373-84.

812 [15] Akira S, Takeda K. Toll-like receptor signalling. Nat Rev Immunol. 2004; 4:
813 499-511.

814 [16] O'Neill LAJ, Golenbock D, Bowie AG. The history of Toll-like
815 receptors-redefining innate immunity. Nat Rev Immunol. 2013; 13: 453-60.

816 [17] Chen R, Zou J, Zhong X, Liu J, Kang R, Tang D. DAMP signaling networks:
817 from receptors to diverse pathophysiological functions. J Adv Res. 2025.

818 [18] Liu JT, Wu SX, Zhang H, Kuang F. Inhibition of MyD88 signaling skews
819 microglia/macrophage polarization and attenuates neuronal apoptosis in the
820 hippocampus after status epilepticus in mice. Neurotherapeutics. 2018; 15: 1093-111.

821 [19] Kaiser T, Feng G. Tmem119-EGFP and Tmem119-CreERT2 transgenic mice for
822 labeling and manipulating microglia. eNeuro. 2019; 6: ENEURO.0448-18.2019.

823 [20] Li C, Wu Z, Zhou L, Shao J, Hu X, Xu W, et al. Temporal and spatial cellular and
824 molecular pathological alterations with single-cell resolution in the adult spinal cord
825 after injury. Signal Transduct Target Ther. 2022; 7: 79.

826 [21] Wang N, Han X, Liu H, Zhao T, Li J, Feng Y, et al. Myeloid differentiation factor
827 88 is up-regulated in epileptic brain and contributes to experimental seizures in rats.
828 Exp Neurol. 2017; 295: 23-35.

829 [22] Griesenauer B, Jiang H, Yang J, Zhang J, Ramadan AM, Egbosiuba J, et al.
830 ST2/MyD88 deficiency protects mice against acute graft-versus-host disease and
831 spares regulatory T cells. J Immunol. 2019; 202: 3053-64.

832 [23] Zhang M, Kleber S, Röhrich M, Timke C, Han N, Tuettenberg J, et al. Blockade
833 of TGF-β signaling by the TGFβR-I kinase inhibitor LY2109761 enhances radiation
834 response and prolongs survival in glioblastoma. Cancer Res. 2011; 71: 7155-67.

835 [24] Loiarro M, Sette C, Gallo G, Ciacci A, Fantò N, Mastroianni D, et al.
836 Peptide-mediated interference of TIR domain dimerization in MyD88 inhibits
837 interleukin-1-dependent activation of NF-κB. J Biol Chem. 2005; 280: 15809-14.

838 [25] Subramanian A, Tamayo P, Mootha VK, Mukherjee S, Ebert BL, Gillette MA, et
839 al. Gene set enrichment analysis: a knowledge-based approach for interpreting
840 genome-wide expression profiles. Proc Natl Acad Sci U S A. 2005; 102: 15545-50.

841 [26] Love MI, Huber W, Anders S. Moderated estimation of fold change and
842 dispersion for RNA-seq data with DESeq2. Genome Biol. 2014; 15: 550.

843 [27] Aibar S, González-Blas CB, Moerman T, Huynh-Thu VA, Imrichova H,

844 Hulselmans G, et al. SCENIC: single-cell regulatory network inference and clustering.
845 Nat Methods. 2017; 14: 1083-6.

846 [28] Skinnider MA, Gautier M, Teo AYY, Kathe C, Hutson TH, Laskaratos A, et al.
847 Single-cell and spatial atlases of spinal cord injury in the Tabulae Paralytica. Nature.
848 2024; 631: 150-63.

849 [29] Basso DM, Fisher LC, Anderson AJ, Jakeman LB, McTigue DM, Popovich PG.
850 Basso Mouse Scale for locomotion detects differences in recovery after spinal cord
851 injury in five common mouse strains. J Neurotrauma. 2006; 23: 635-59.

852 [30] Hamers FPT, Lankhorst AJ, van Laar TJ, Veldhuis WB, Gispen WH. Automated
853 quantitative gait analysis during overground locomotion in the rat: its application to
854 spinal cord contusion and transection injuries. J Neurotrauma. 2001; 18: 187-201.

855 [31] Steward O, Zheng B, Tessier-Lavigne M. False resurrections: distinguishing
856 regenerated from spared axons in the injured central nervous system. J Comp Neurol.
857 2003; 459: 1-8.

858 [32] Yu B, Zhang Y, Yang Y, Yang S, Wu H, Gao X, et al. Neonatal-inspired
859 reprogramming of microglial pan-programmed cell death enhances regeneration in
860 adult spinal cord injury. Research (Wash D C). 2025; 8: 0759.

861 [33] Bedolla A, Wegman E, Weed M, Stevens MK, Ware K, Paranjpe A, et al. Adult
862 microglial TGFβ1 is required for microglia homeostasis via an autocrine mechanism
863 to maintain cognitive function in mice. Nat Commun. 2024; 15: 5306.

864 [34] Fang RH, Kroll AV, Gao W, Zhang L. Cell membrane coating nanotechnology.

865 Adv Mater. 2018; 30: e1706759.

866 [35] Al Mamun A, Wu Y, Monalisa I, Jia C, Zhou K, Munir F, et al. Role of pyroptosis
867 in spinal cord injury and its therapeutic implications. J Adv Res. 2021; 28: 97-109.

868 [36] Yan H, Zhang D, Wei Y, Ni H, Liang W, Zhang H, et al. Inhibition of myeloid
869 differentiation primary response protein 88 provides neuroprotection in early brain
870 injury following experimental subarachnoid hemorrhage. Sci Rep. 2017; 7: 15797.

871 [37] Kigerl KA, Popovich PG. Toll-like receptors in spinal cord injury. Curr Top
872 Microbiol Immunol. 2009; 336: 121-36.

873 [38] Rust R, Kaiser J. Insights into the dual role of inflammation after spinal cord
874 injury. J Neurosci. 2017; 37: 4658-60.

875 [39] Hu X, Xu Y, Zhang H, Li Y, Wang X, Xu C, et al. Role of necroptosis in
876 traumatic brain and spinal cord injuries. J Adv Res. 2022; 40: 125-34.

877 [40] Greenhalgh AD, David S. Differences in the phagocytic response of microglia
878 and peripheral macrophages after spinal cord injury and its effects on cell death. J
879 Neurosci. 2014; 34: 6316-22.

880 [41] Gensel JC, Zhang B. Macrophage activation and its role in repair and pathology
881 after spinal cord injury. Brain Res. 2015; 1619: 1-11.

882 [42] Schwab JM, Zhang Y, Kopp MA, Brommer B, Popovich PG. The paradox of
883 chronic neuroinflammation, systemic immune suppression, and autoimmunity after
884 traumatic spinal cord injury. Exp Neurol. 2014; 258: 121-9.

885 [43] Silver J, Miller JH. Regeneration beyond the glial scar. Nat Rev Neurosci. 2004;

886 5: 146-56.

887 [44] Fan B, Wei Z, Yao X, Shi G, Cheng X, Zhou X, et al. Microenvironment
888 imbalance of spinal cord injury. Cell Transplant. 2018; 27: 853-66.

889 [45] Burda JE, Sofroniew MV. Reactive gliosis and the multicellular response to CNS
890 damage and disease. Neuron. 2014; 81: 229-48.

891 [46] Anderson MA, Burda JE, Ren Y, Ao Y, O'Shea TM, Kawaguchi R, et al.
892 Astrocyte scar formation aids central nervous system axon regeneration. Nature. 2016;
893 532: 195-200.

894 [47] Bradbury EJ, Burnside ER. Moving beyond the glial scar for spinal cord repair.
895 Nat Commun. 2019; 10: 3879.

896 [48] Cregg JM, DePaul MA, Filous AR, Lang BT, Tran A, Silver J. Functional
897 regeneration beyond the glial scar. Exp Neurol. 2014; 253: 197-207.

898 [49] Li Y, He X, Kawaguchi R, Zhang Y, Wang Q, Monavarfeshani A, et al.
899 Microglia-organized scar-free spinal cord repair in neonatal mice. Nature. 2020; 587:
900 613-8.

901 [50] Benowitz LI, Popovich PG. Inflammation and axon regeneration. Curr Opin
902 Neurol. 2011; 24: 577-83.

903 [51] Sankowski R, Böttcher C, Masuda T, Geirsdottir L, Sagar, Sindram E, et al.
904 Mapping microglia states in the human brain through the integration of
905 high-dimensional techniques. Nat Neurosci. 2019; 22: 2098-110.

906 [52] Wang J, Xu L, Lin W, Yao Y, Li H, Shen G, et al. Single-cell transcriptome

907 analysis reveals the immune heterogeneity and the repopulation of microglia by Hif1α
908 in mice after spinal cord injury. Cell Death Dis. 2022; 13: 432.

909 [53] Tansley S, Uttam S, Ureña Guzmán A, Yaqubi M, Pacis A, Parisien M, et al.
910 Single-cell RNA sequencing reveals time- and sex-specific responses of mouse spinal
911 cord microglia to peripheral nerve injury and links ApoE to chronic pain. Nat
912 Commun. 2022; 13: 843.

913 [54] Butovsky O, Jedrychowski MP, Moore CS, Cialic R, Lanser AJ, Gabriely G, et al.
914 Identification of a unique TGF-β-dependent molecular and functional signature in
915 microglia. Nat Neurosci. 2014; 17: 131-43.

916 [55] Zöller T, Schneider A, Kleimeyer C, Masuda T, Potru PS, Pfeifer D, et al.
917 Silencing of TGFβ signalling in microglia results in impaired homeostasis. Nat
918 Commun. 2018; 9: 4011.

919 [56] Massagué J. TGFβ signalling in context. Nat Rev Mol Cell Biol. 2012; 13:
920 616-30.

921 [57] Estrada LD, Oliveira-Cruz L, Cabrera D. Transforming growth factor beta type I
922 role in neurodegeneration: implications for Alzheimer's disease. Curr Protein Pept Sci.
923 2018; 19: 1180-8.

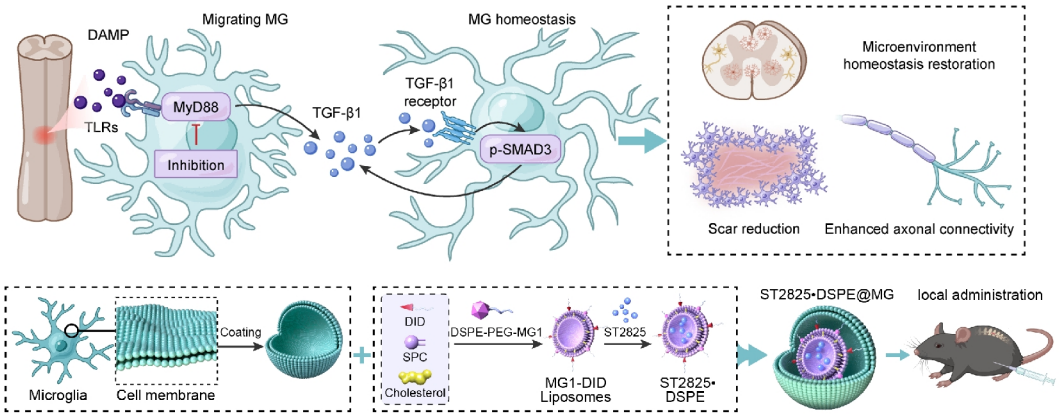

924

925 **Graphical Abstract**

926 Microglia-targeted ST2825·DSPE@MG nanoparticles inhibit microglial MyD88 via

927 TGF-β-dependent signaling, restoring microenvironment homeostasis, reducing scar

928 formation, and enhancing axonal connectivity.

929

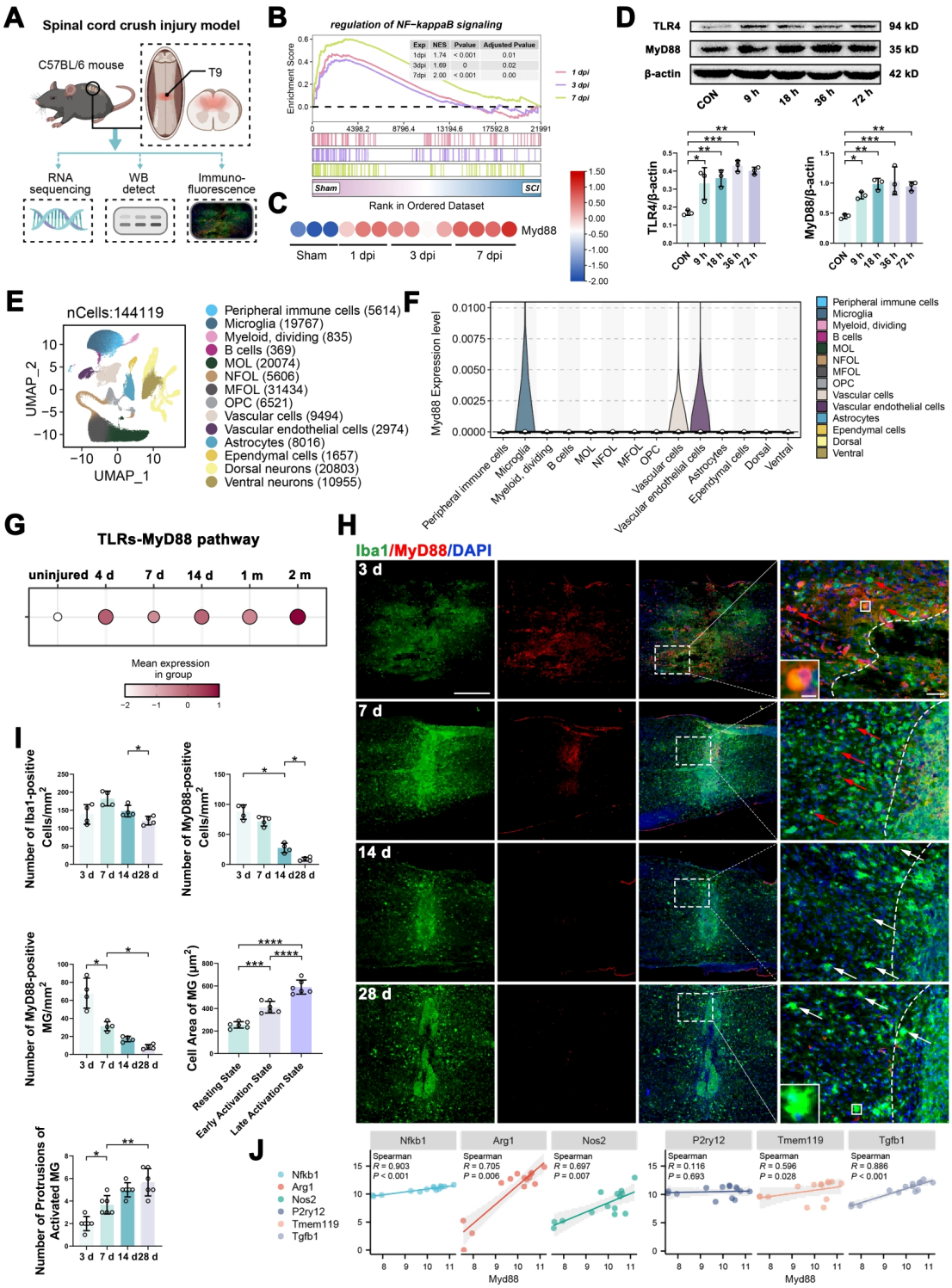

930

931 **Figure 1.** MyD88 signaling is rapidly induced and predominantly engaged in

932 microglia after SCI. (A) Schematic of the forceps-mediated spinal cord crush model

933 and workflow for RNA-seq, immunoblotting, and immunofluorescence. (B) GSEA

934 showing enrichment of the "regulation of NF-κB signaling" gene set at 1, 3, and 7 dpi.

(C) *Myd88* expression ranking in bulk RNA-seq datasets from sham and SCI spinal cord tissues at 1, 3, and 7 dpi. (D) Representative immunoblots and densitometric quantification of TLR4 and MyD88 in injured spinal cord tissue across the acute phase; normalized to β-actin. Data are mean ± SD; n = 3 mice/group; one-way ANOVA with Tukey's post hoc test. (E) UMAP of cells from the Tabulae Paralytica SCI single-cell atlas colored by *Myd88* expression. (F) Violin plots of *Myd88* expression across annotated cell populations. (G) AUCell scoring of TLR-MyD88 pathway activity in microglia over time. (H) Representative longitudinal sections at 3, 7, 14, and 28 dpi stained for MyD88 (red) and Iba1 (green); DAPI (blue). Dashed lines indicate lesion boundaries; boxed regions show higher magnification. (I) Quantification of $Iba1^+$ cell density, $MyD88^+Iba1^+$ microglial density, soma area, and protrusion number at 3, 7, 14, and 28 dpi. Data are mean ± SD; n = 4 mice/group; one-way ANOVA or two-way repeated-measures ANOVA followed by Tukey's post hoc test. MG: microglia. (J) Spearman correlations of expression level of mRNA FPKM between *Myd88* and microglial marker genes (*P2ry12*, *Tmem119*, *Nos2*, *Nfkb1*, *Arg1*, *Tgfb1*) during the acute stage. Correlation analysis was based on bulk RNA-seq data from lesion-centered spinal cord tissues at 1, 3, and 7 dpi (n = 4, 5, and 5 independent samples per time point, respectively). Scale bars: 500 μm (overview), 50 μm (insets), 10 μm (single-cell views). Statistical significance: $*p < 0.05$, $**p < 0.01$, $***p < 0.001$, $****p < 0.0001$; ns, not significant.

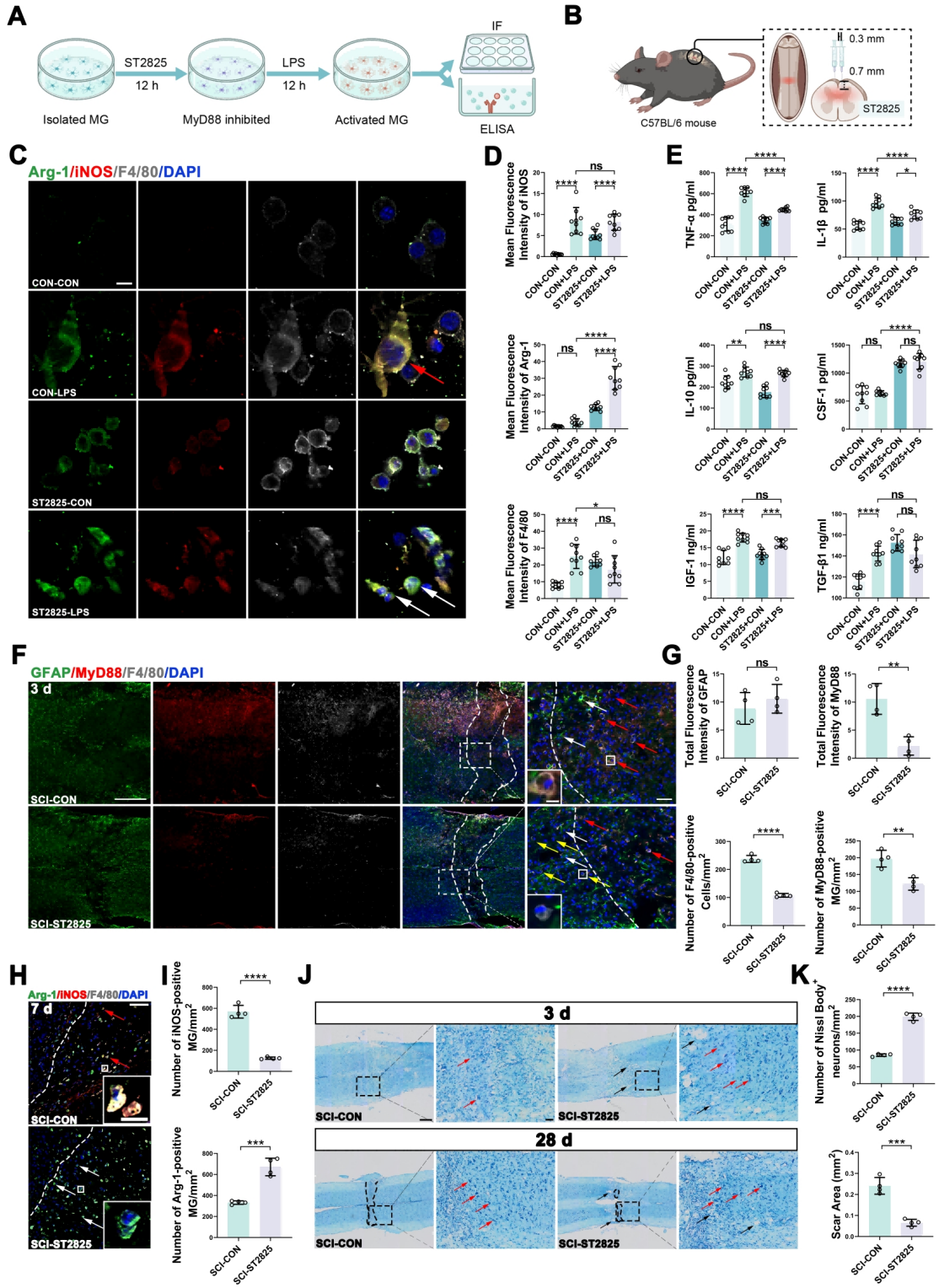

Figure 2. ST2825 reprograms microglial inflammatory output *in vitro* and *in vivo*. (A) *In vitro* workflow for primary microglia: ST2825 pretreatment followed by LPS stimulation. (B) *In vivo* design: bilateral intraspinal ST2825 injection immediately

after SCI. (C) Representative primary microglia stained for Arg-1 (green), iNOS (red), F4/80 (white), and DAPI (blue). Scale bar: 10 μm. (D) Quantification of iNOS, Arg-1, and F4/80 mean fluorescence intensity in primary microglia. Data are mean ± SD; one-way ANOVA with Tukey's post hoc test. (E) Multiplex ELISA quantification of secreted TNF-α, IL-1β, IL-10, CSF-1, TGF-β1, and IGF-1 levels. Data are mean ± SD; one-way ANOVA with Tukey's post hoc test. (F) Representative spinal cord sections at 3 dpi stained for GFAP (green), MyD88 (red), F4/80 (white), and DAPI (blue). (G) Quantification of GFAP, MyD88 fluorescence intensity, densities of $F4/80^+$ cells and $MyD88^+$ microglia at 3 dpi. Data are mean ± SD; n = 4 mice/group; unpaired two-tailed *t*-test. (H) Representative sections at 7 dpi stained for Arg-1 (green), iNOS (red), F4/80 (white), and DAPI (blue). (I) Quantification of $iNOS^+$ and $Arg\text{-}1^+$ microglia at 7 dpi. Data are mean ± SD; n = 4 mice/group; unpaired two-tailed *t*-test. (J) Representative Nissl staining at 3 and 28 dpi. Scale bars: 400 μm (overview) and 100 μm (enlarged). (K) Quantification of Nissl body-positive neurons at 3 dpi and scar area at 28 dpi. Data are mean ± SD; n = 4 mice/group; unpaired two-tailed *t*-test. Scale bars: 500 μm (overview), 50 μm (insets), 10 μm (single-cell views) unless otherwise indicated. Statistical significance: $*p < 0.05$, $**p < 0.01$, $***p < 0.001$, $****p < 0.0001$; ns, not significant.

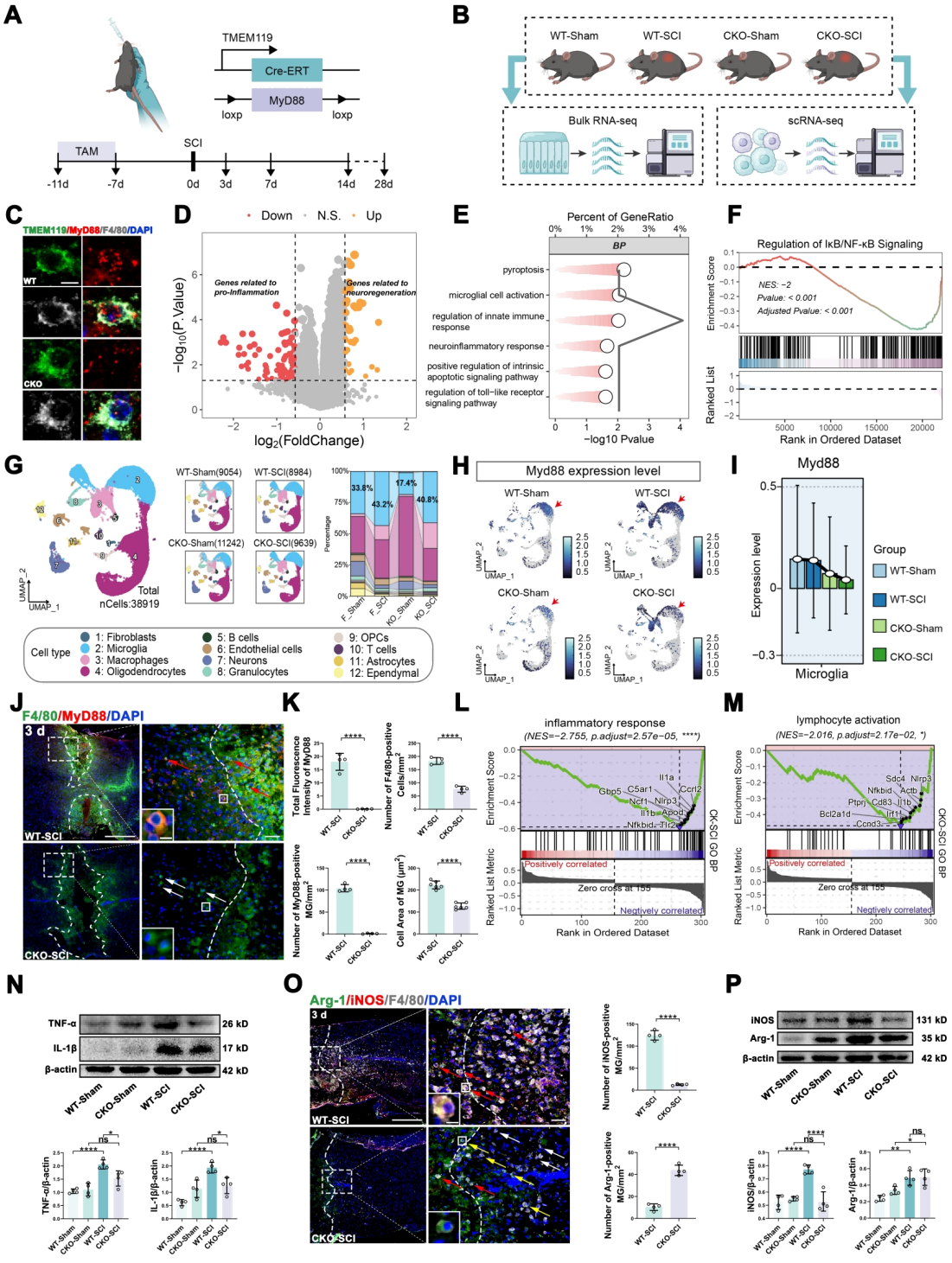

Figure 3. Microglia-specific MyD88 deletion suppresses inflammatory programs and accelerates recovery of homeostasis after SCI. (A) Breeding strategy for *Tmem119*^{CreERT2};*Myd88*$^{fl/fl}$ mice and tamoxifen induction timeline. (B) Experimental design for bulk RNA-seq and scRNA-seq at 3 dpi in WT and cKO mice under sham

or SCI conditions. (C) Representative immunofluorescence at 3 dpi showing TMEM119 (green), MyD88 (red), F4/80 (white), and DAPI (blue). Scale bar: 5 μm. (D) Volcano plot of DEGs (cKO-SCI vs. WT-SCI) from bulk RNA-seq. (E) Functional enrichment of DEGs highlighting reduced immune activation and TLR signaling in cKO-SCI. (F) GSEA showing depletion of "Regulation of IκB/NF-κB signaling" in cKO-SCI. (G) UMAP of 38,919 cells from scRNA-seq showing 12 major cell types and group-wise proportions. (H) Feature plots of *Myd88* expression across groups. (I) Quantification of *Myd88* expression in microglia across groups. (J) Representative sections at 3 dpi stained for F4/80 (green), MyD88 (red), and DAPI (blue). Dashed lines indicate lesion boundaries; boxed regions show higher magnification. (K) Quantification of MyD88 fluorescence intensity and $F4/80^+$ cell parameters within the lesion region. Data are mean ± SD; n = 4 mice/group; unpaired two-tailed *t*-test. (L-M) GSEA showing reduced enrichment of inflammatory response and lymphocyte activation gene sets in cKO-SCI microglia. (N) Representative immunoblots and quantification of TNF-α and IL-1β at 3 dpi; normalized to β-actin. Data are mean ± SD; n = 4 mice/group; one-way ANOVA with Tukey's post hoc test. (O) Representative sections at 3 dpi stained for Arg-1 (green), iNOS (red), F4/80 (white), and DAPI (blue). Data are mean ± SD; n = 4 mice/group; unpaired two-tailed *t*-test. (P) Representative immunoblots and quantification of iNOS and Arg-1; normalized to β-actin. Data are mean ± SD; n = 4 mice/group; one-way ANOVA with Tukey's post hoc test. Scale bars: 500 μm (overview), 50 μm (insets), 10 μm

(single-cell views) unless otherwise indicated. Statistical significance: *$p < 0.05$, **$p < 0.01$, ****$p < 0.0001$; ns, not significant.

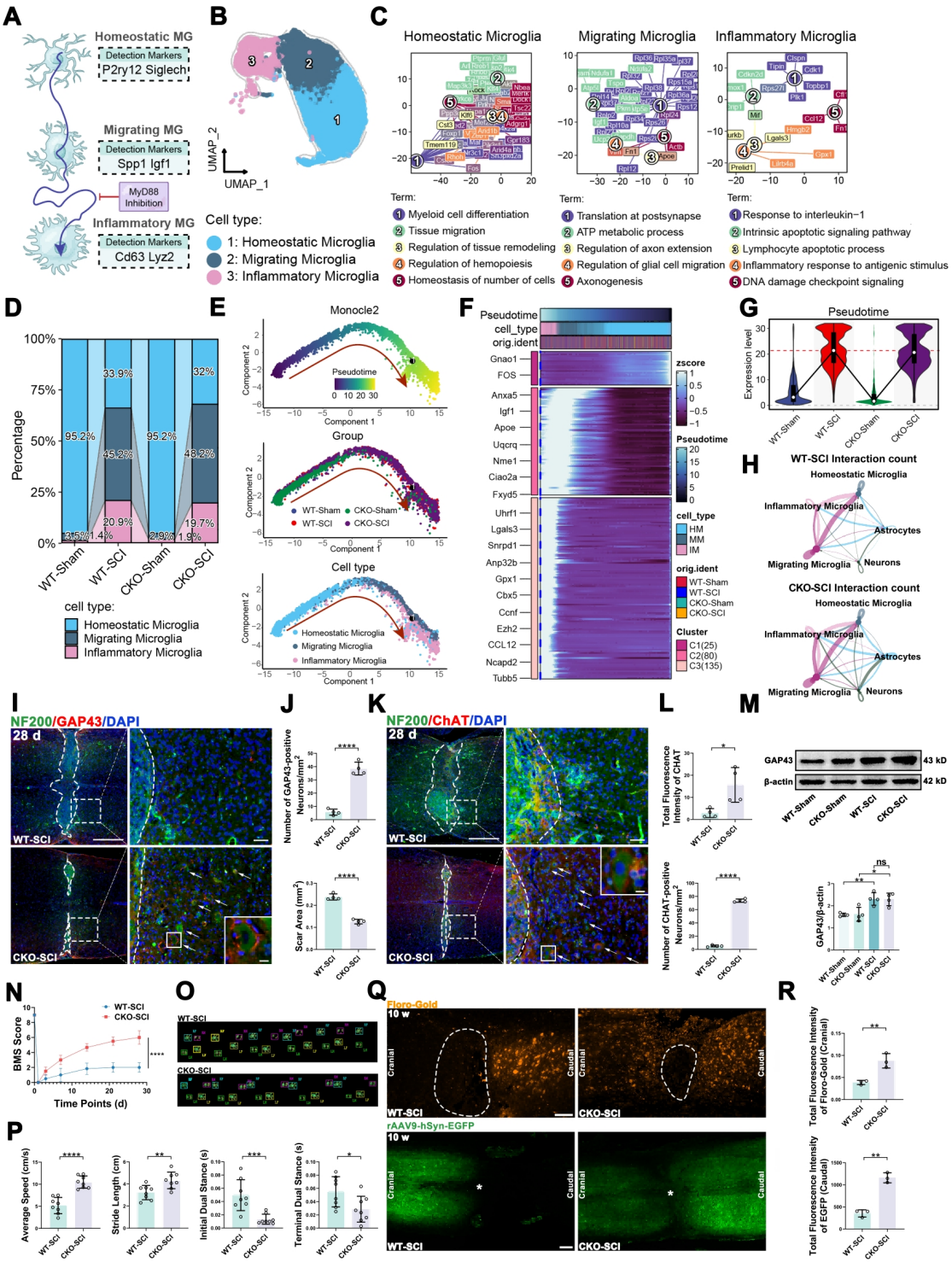

Figure 4. Microglial MyD88 deletion shifts injury-activated microglial states and improves tissue repair, axonal growth, and locomotor recovery. (A) Schematic of microglial state transitions after SCI and the proposed impact of MyD88 inhibition. (B) UMAP of microglia showing three states: homeostatic (*P2ry12*, *Siglech*),

migrating (*Spp1*, *Igf1*), and inflammatory (*Cd63*, *Lyz2*). (C) Representative functional enrichment terms for each microglial state. (D) State proportions across groups during the acute phase. (E) Monocle2 pseudotime trajectories. (F) Heatmap of genes dynamically regulated along pseudotime. (G) Distribution of cells along pseudotime across groups. (H) Ligand-receptor interaction analysis of intercellular communication among homeostatic, inflammatory, migrating microglia, neurons and astrocytes in WT-SCI and cKO-SCI mice. (I) Representative sections at 28 dpi stained for NF200 (green), GAP43 (red), and DAPI (blue). (J) Quantification of $GAP43^+$ neurons and scar area at 28 dpi. Data are mean ± SD; n = 4 mice/group; unpaired two-tailed *t*-test. (K) Representative ventral horn sections at 28 dpi stained for ChAT (red), NF200 (green), and DAPI (blue). (L) Quantification of $ChAT^+NF200^+$ neurons at 28 dpi. Data are mean ± SD; n = 4 mice/group; unpaired two-tailed *t*-test. (M) Representative immunoblots and quantification of GAP43 at 28 dpi; normalized to β-actin. Data are mean ± SD; n = 4 mice/group; one-way ANOVA with Tukey's post hoc test. (N) BMS scores after SCI. Data are mean ± SD; n = 6 mice/group; two-way repeated-measures ANOVA. (O) Representative CatWalk footprints at 28 dpi. (P) Quantification of CatWalk gait parameters at 28 dpi. Data are mean ± SD; n = 8 mice/group; unpaired two-tailed *t*-test. (Q) Representative images of retrograde Fluoro-Gold and anterograde rAAV9-hSyn-EGFP tracing. Dashed lines indicate lesion borders; asterisks indicate scar regions. Scale bars: 100 μm. (R) Quantification of Fluoro-Gold signal cranial to the lesion and EGFP signal caudal to the lesion. Data are mean ± SD; n = 3 mice/group; unpaired two-tailed *t*-test. Scale bars: 500 μm

(overview), 50 μm (insets), 10 μm (single-cell views) unless otherwise indicated. Statistical significance: *$p < 0.05$, **$p < 0.01$, ***$p < 0.001$, ****$p < 0.0001$; ns, not significant.

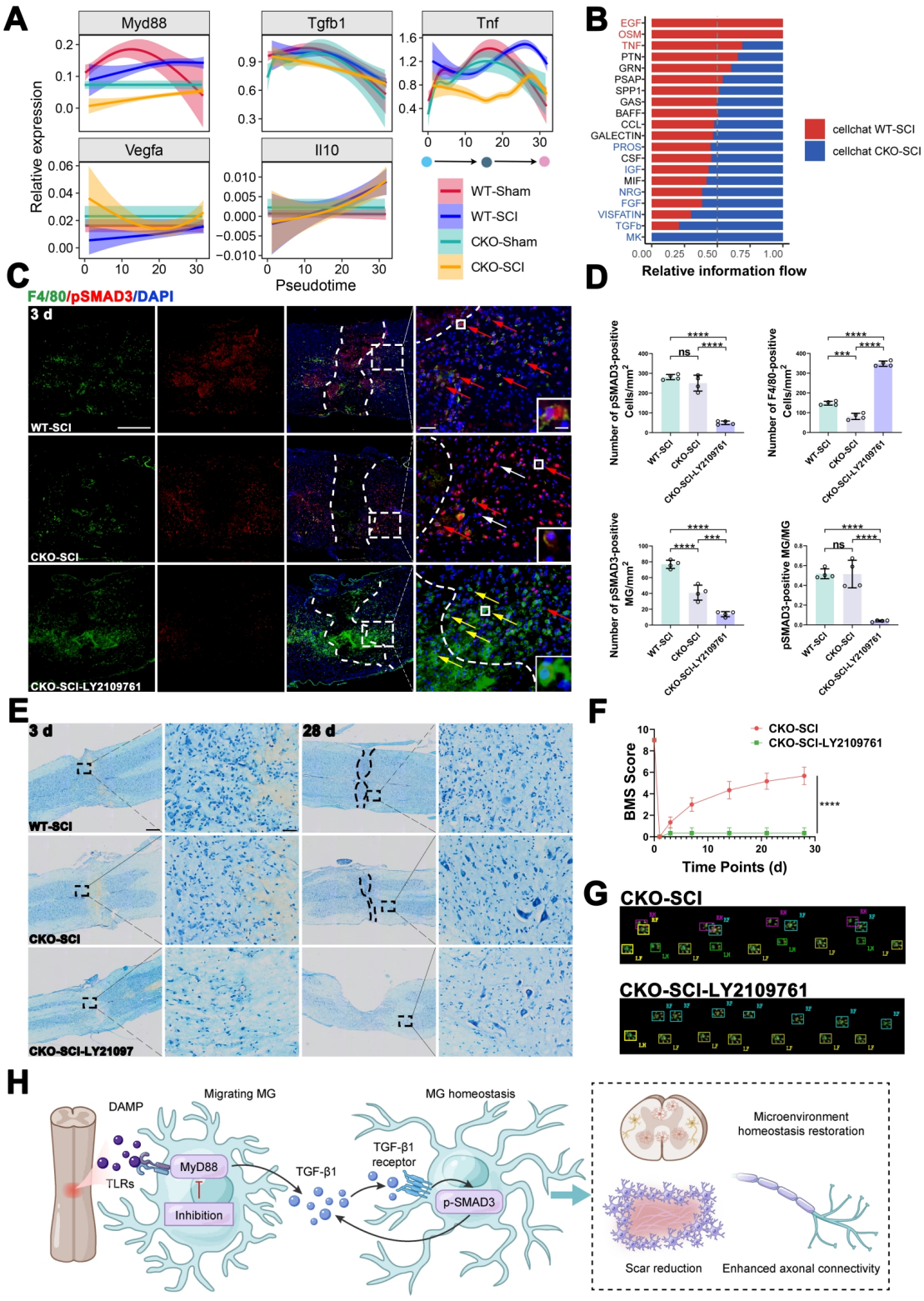

Figure 5. TGF-β1 receptor/pSMAD3 signaling is required for microglial state transition and functional recovery in microglial MyD88 cKO mice. (A) Smoothed expression of *Myd88*, *Tgfb1*, *Tnf*, *Vegfa*, and *Il10* along microglial pseudotime across

groups. (B) CellChat analysis of differential intercellular communication networks between WT-SCI and cKO-SCI groups. Upregulated signaling pathways in cKO-SCI (e.g., FGF, TGF-β) and WT-SCI (e.g., EGF, OSM, TNF) are shown. Bar length represents the relative signaling strength. (C) Representative sections at 3 dpi stained for F4/80 (green), pSMAD3 (red), and DAPI (blue). Dashed lines indicate lesion regions; boxed regions show higher magnification. (D) Quantification of $pSMAD3^{+}$ cells and microglia responses at 3 dpi. Data are mean ± SD; n = 4 mice/group; one-way ANOVA with Tukey's post hoc test. (E) Representative Nissl staining at 3 and 28 dpi. Scale bars: 400 μm (overview), 40 μm (enlarged). (F) BMS scores comparing cKO-SCI and cKO-SCI + LY2109761 groups. Data are mean ± SD; n = 6 mice/group; two-way repeated-measures ANOVA. (G) Representative CatWalk footprints at 28 dpi. (H) Working model linking microglial MyD88 suppression to TGF-β-dependent repair. Scale bars: 500 μm (overview), 50 μm (insets), 10 μm (single-cell views) unless otherwise indicated. Statistical significance: ***$p < 0.001$, ****$p < 0.0001$; ns, not significant.

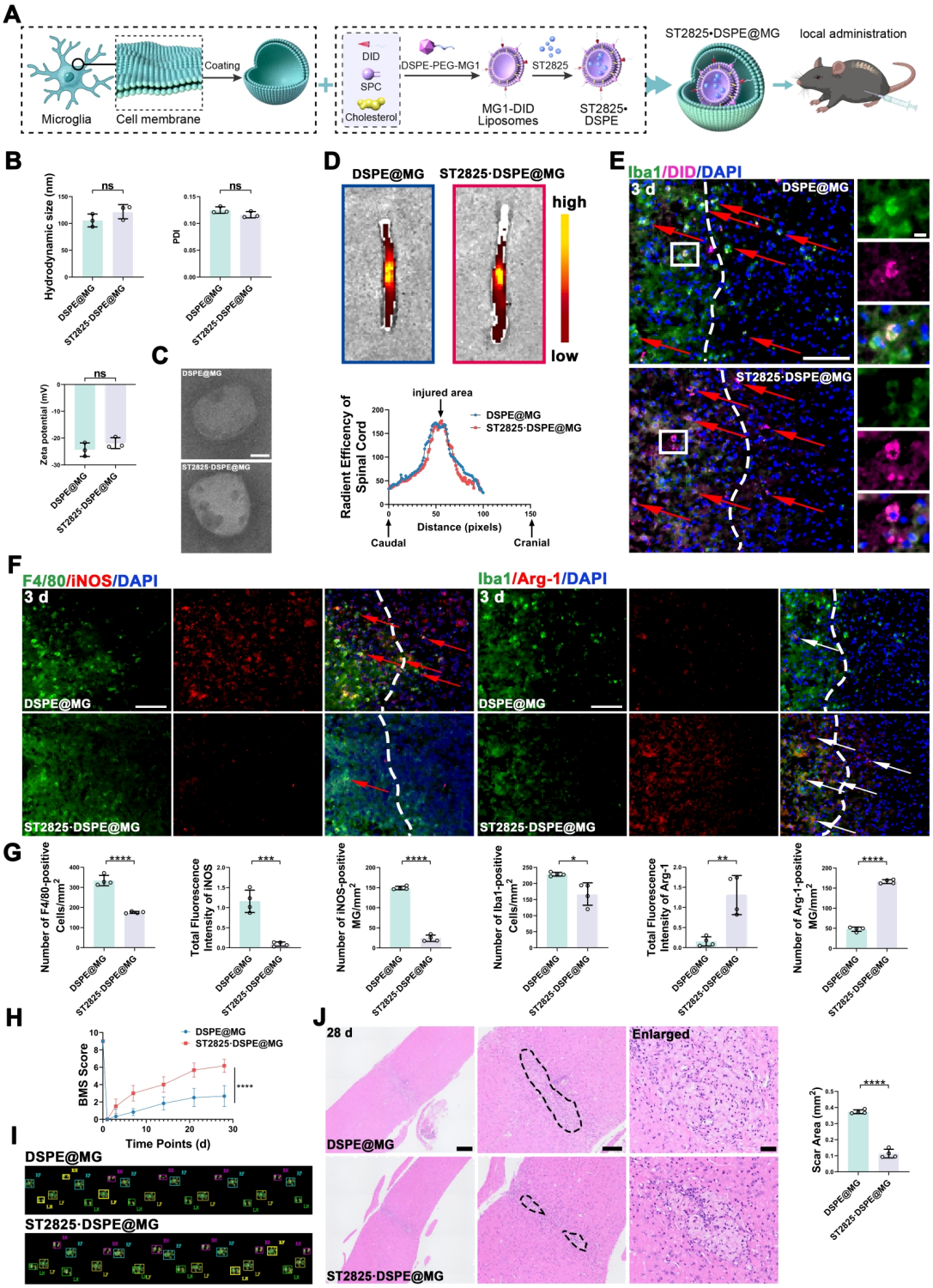

Figure 6. Microglia-targeted ST2825·DSPE@MG nanoparticles show microglia uptake and therapeutic efficacy after SCI. (A) Schematic of ST2825·DSPE@MG fabrication. (B) DLS characterization of DSPE@MG and ST2825·DSPE@MG (hydrodynamic diameter, PDI, zeta potential). Data are mean ± SD; n = 3; unpaired

two-tailed *t*-test. (C) Representative TEM images showing core-shell morphology. Scale bars: 50 nm. (D) *Ex vivo* fluorescence imaging at 3 days after administration of DiD-labeled nanoparticles and radiant efficiency profiles along the rostrocaudal axis. (E) Images showing colocalization of DiD-labeled nanoparticles with $Iba1^+$ microglia at the lesion boundary. Scale bars: 100 μm (overview) and 10 μm (single-cell views). (F) Representative sections at 3 dpi stained for F4/80 (green) and iNOS (red) (left), and Iba1 (green) and Arg-1 (red) (right); DAPI (blue). Scale bars: 100 μm. (G) Quantification of lesion-region microglia and markers at 3 dpi. Data are mean ± SD; n = 4 mice/group; unpaired two-tailed *t*-test. (H) BMS scores after SCI. Data are mean ± SD; n = 6 mice/group; two-way repeated-measures ANOVA. (I) Representative CatWalk footprints at 28 dpi. (J) Representative H-E staining at 28 dpi and quantification of scar area. Data are mean ± SD; n = 4 mice/group; unpaired two-tailed *t*-test. Scale bars: 400 μm (overview), 100 μm (injury area), and 40 μm (enlarged). Statistical significance: $*p < 0.05$, $**p < 0.01$, $***p < 0.001$, $****p < 0.0001$; ns, not significant.

Table S1.

Antibodies used in immunohistochemistry (IF) and Western blotting (WB)

Antigen	Host Species	Applicati-on	Vendor	Catalog No.	Dilution (IF)	Dilution (WB)
Primary Antibodies						
MyD88	Mouse	IF, WB	Proteintech	67969-1-Ig	1:400	1:2000
Iba1	Rabbit	IF	Wako	019-19741	1:800	—
F4/80	Rat	IF	Invitrogen	14-4801-82	1:100	—
GFAP	Mouse	IF	Millipore	MAB360	1:1000	—
iNOS (NOS2)	Rabbit	IF, WB	Proteintech	22226-1-AP	1:200	1:1000
Arg-1 (Arginase-1)	Mouse	IF, WB	Invitrogen	MA5-31577	1:200	1:1000
TMEM119	Rabbit	IF	Proteintech	27585-1-AP	1:400	—
pSMAD3	Rabbit	IF	Abcam	ab52903	1:200	—
NF200 (Neurofilament-H)	Mouse	IF	Proteintech	60331-1-Ig	1:400	—
GAP43	Rabbit	IF, WB	Proteintech	16971-1-AP	1:400	1:2000
ChAT	Rabbit	IF	Proteintech	20747-1-AP	1:200	—
TUJ1 (β-III tubulin)	Mouse	IF	Proteintech	66240-1-Ig	1:400	—
Synaptophysin (Syn)	Rabbit	IF	Proteintech	17785-1-AP	1:200	—
TLR4	Rabbit	WB	Abgent	AP1504a	—	1:500
TNF-α	Rabbit	WB	Abcam	ab6671	—	1:200
IL-1β	Mouse	WB	Cell Signaling	CS12242	—	1:1000
β-actin	Mouse	WB	Sigma-Aldrich	A5441	—	1:1000
Secondary Antibodies						
Donkey anti-Rabbit IgG, Alexa Fluor 488	Donkey	IF	Invitrogen	A21206	1:1000	—
Donkey anti-Rabbit IgG, Alexa Fluor 594	Donkey	IF	Invitrogen	A21207	1:1000	—
Goat anti-Mouse IgG, Alexa Fluor 488	Goat	IF	Invitrogen	A11001	1:1000	—
Goat anti-Mouse IgG, Alexa Fluor 594	Goat	IF	Invitrogen	A11032	1:1000	—
Goat Anti-Rat IgG, Alexa Fluor 647	Goat	IF	Abcam	ab150159	1:800	—
Goat anti-Rabbit IgG, HRP-conjugated	Goat	WB	Zhuangzhibio	EK020	—	1:1000
Goat anti-Mouse IgG, HRP-conjugated	Goat	WB	Zhuangzhibio	EK010	—	1:1000

Table S2

Corresponding cell numbers and proportions for each microglial subtype

Group	Total	Homeostatic	Migrating	Inflammatory
WT-Sham	3011	2867 (95.2%)	105 (3.5%)	42 (1.4%)
WT-SCI	3860	1309 (33.9%)	1745 (45.2%)	807 (20.9%)
cKO-Sham	1929	1836 (95.2%)	56 (2.9%)	37 (1.9%)
cKO-SCI	3882	1242 (32.0%)	1871 (48.2%)	765 (19.7%)

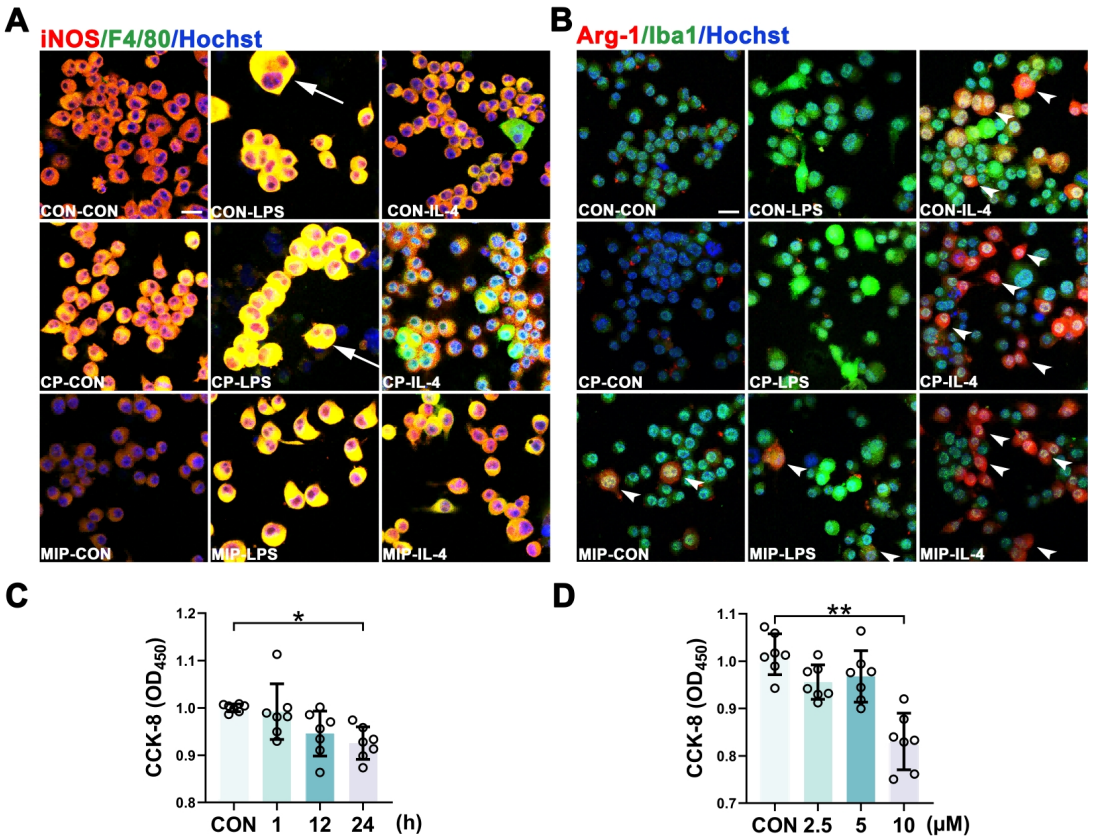

Figure S1. MyD88 inhibitory peptide attenuates LPS-induced iNOS and increases Arg-1^{+} cells in N9 microglia. (A) Representative N9 microglia stained for iNOS (red) and F4/80 (green); Hoechst (blue). (B) Representative N9 microglia stained for Arg-1 (red) and Iba1 (green); Hoechst (blue). (C) CCK-8 assay for microglia treated with ST2825 over different time periods (1, 12, and 24 h). (D) CCK-8 assay for microglia treated with different concentrations of ST2825 (2.5, 5, and 10 μM). Data are mean ± SD; one-way ANOVA with Tukey's post hoc test. Scale bars: 20 μm. Statistical significance: *$p < 0.05$, **$p < 0.01$.

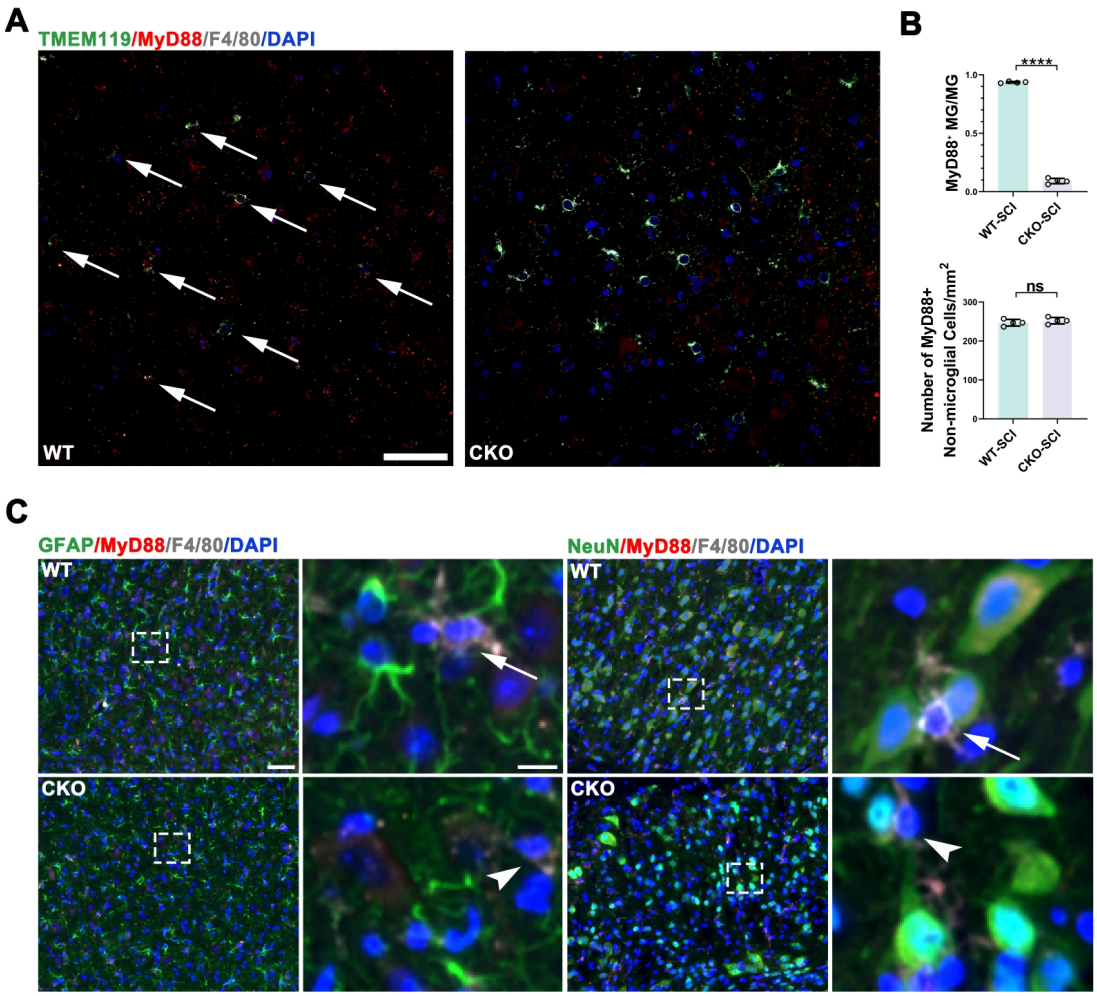

Figure S2. Validation of microglia-specific MyD88 deletion in cKO mice. (A) Representative sections of uninjured spinal cords stained for TMEM119 (green), MyD88 (red), F4/80 (white), and DAPI (blue). Arrows indicate the colocalization of microglial markers with MyD88 in WT mice, which is largely lost in cKO mice. (B) Quantification of MyD88^{+}TMEM119^{+}F4/80^{+} cells and MyD88^{+}TMEM119^{-}F4/80^{-} cells in spinal cord. (C) Representative images of spinal cords stained for MyD88 (red) and F4/80 (white) along with GFAP (green) or NeuN (green). Arrows indicate MyD88 colocalization within F4/80^{+} cells. Arrowheads indicate F4/80^{+} cells in the cKO-SCI group lacking MyD88 expression. Data are mean ± SD; n = 4 mice/group; unpaired two-tailed *t*-test. Scale bars: 50 μm (overview), 10 μm (single-cell views). Statistical

significance: ****$p < 0.0001$; ns, not significant.

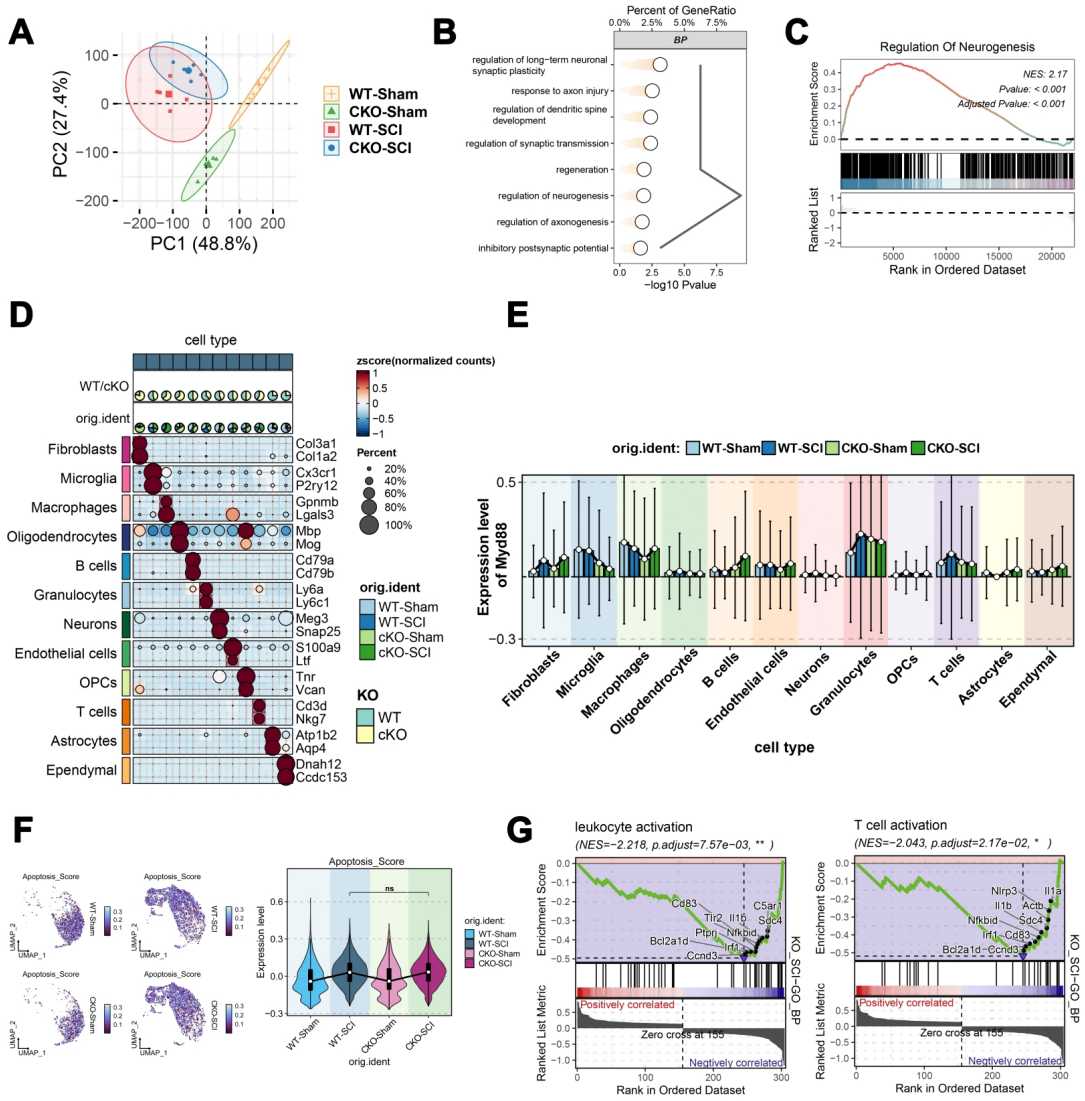

Figure S3. Bulk and single-cell transcriptomic analyses after microglial MyD88 deletion. (A) PCA of bulk RNA-seq profiles from sham and 3 dpi spinal cords. (B) GO terms enriched among upregulated genes in cKO-SCI versus WT-SCI. (C) GSEA plot for “regulation of neurogenesis” in cKO-SCI. (D) Dot plot of canonical markers used to annotate major cell populations in scRNA-seq. (E) MyD88 expression across major cell types in scRNA-seq across groups. (F) UMAP feature plots and violin plots showing the distribution and quantification of the apoptosis score across experimental groups. (G) GSEA plot showing lower enrichment of immune activation programs in

cKO-SCI microglia.

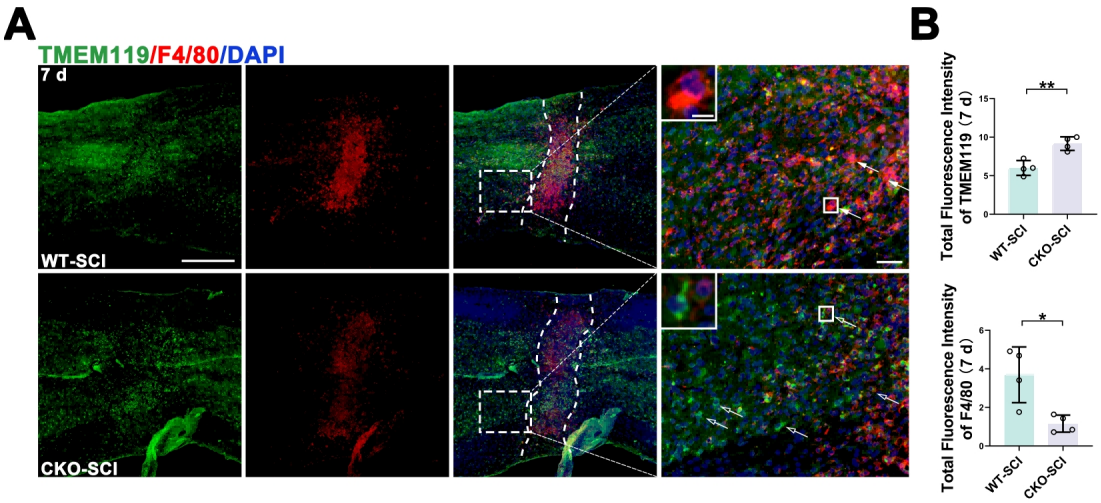

Figure S4. Accelerated recovery of microglia homeostasis in cKO mice after SCI. (A) Representative longitudinal sections at 7 dpi stained for TMEM119 (green) and F4/80 (red); DAPI (blue). (B) Quantification of TMEM119 and F4/80 fluorescence intensity at 7 dpi. Data are mean ± SD; n = 4 mice/group; unpaired two-tailed *t*-test. Scale bars: 500 µm (overview), 50 µm (insets), 10 µm (single-cell views). Statistical significance: **p* < 0.05, ***p* < 0.01.

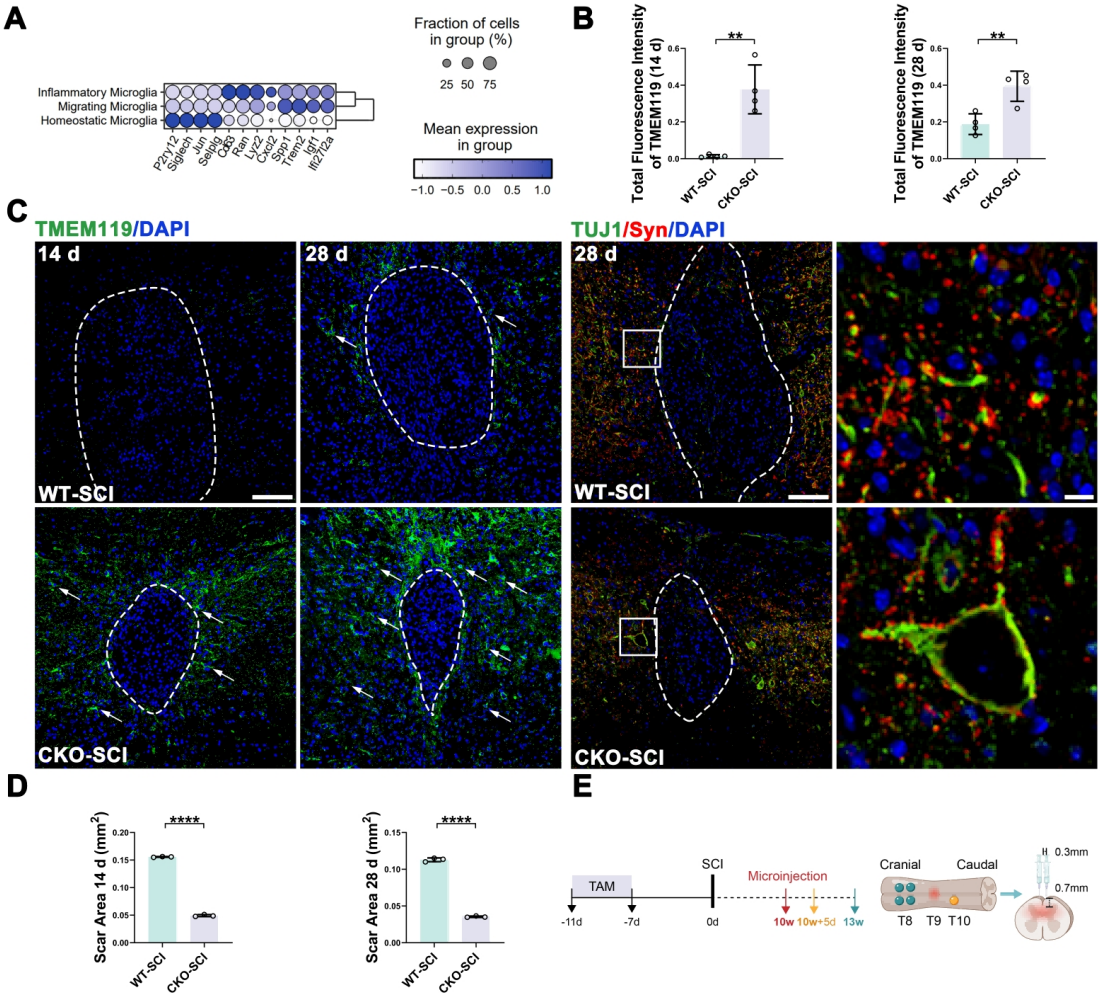

Figure S5. MyD88 cKO promotes microglial homeostasis and tissue repair after SCI. (A) Dot plot of representative marker genes across homeostatic, migrating, and inflammatory microglial states. Dot size indicates the fraction of expressing cells; color intensity indicates scaled average expression. (B-D) Sustained TMEM119 signal and reduced scar area in microglial MyD88 cKO mice. Data are mean ± SD; n = 4 mice/group; unpaired two-tailed *t*-test. Scale bars: 100 μm (overview), 10 μm (insets). Statistical significance: $^{**}p < 0.01$, $^{****}p < 0.0001$. (E) Schematic of tamoxifen induction, SCI, tracer delivery, and tissue collection. rAAV9-hSyn-EGFP was injected cranial to the lesion (four sites), and Fluoro-Gold was injected caudal to the lesion (one site). Coordinates relative to the dorsal surface are indicated (0.3 mm lateral, 0.7

mm depth).

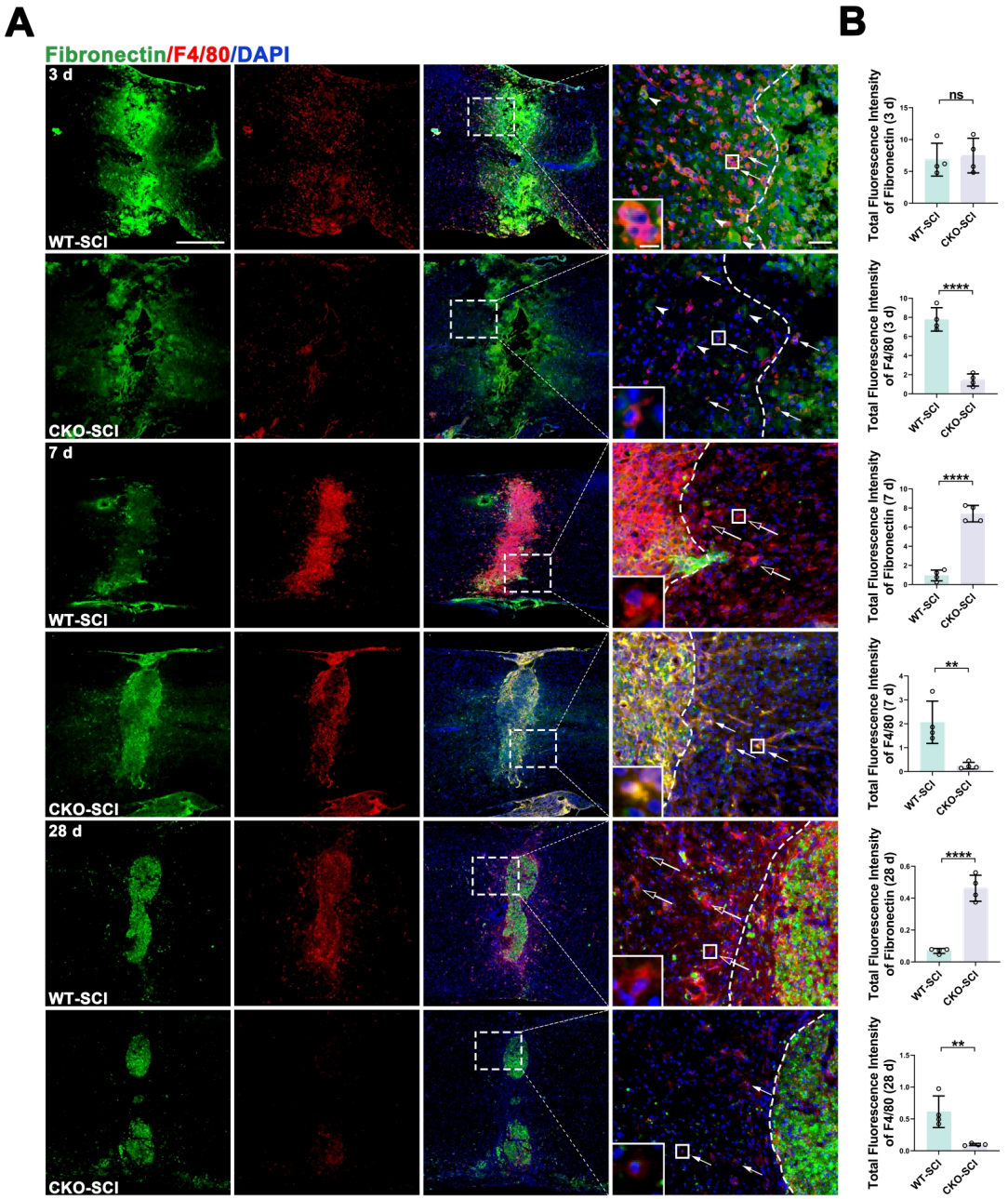

Figure S6. Fibronectin reveals sustained perilesional expression in cKO-SCI microglia compared with WT-SCI. (A) Representative longitudinal sections at 3, 7, and 28 dpi stained for fibronectin (green) and F4/80 (red); DAPI (blue). (B) Quantification of total fluorescence intensity of fibronectin and F4/80 at 3, 7, and 28 dpi. Data are mean ± SD; n = 4 mice/group; unpaired two-tailed *t*-test. Scale bars: 500 µm (overview), 50 µm (insets), 10 µm (single-cell views). Statistical significance: ***p*

1144 < 0.01, ****$p < 0.0001$; ns, not significant.

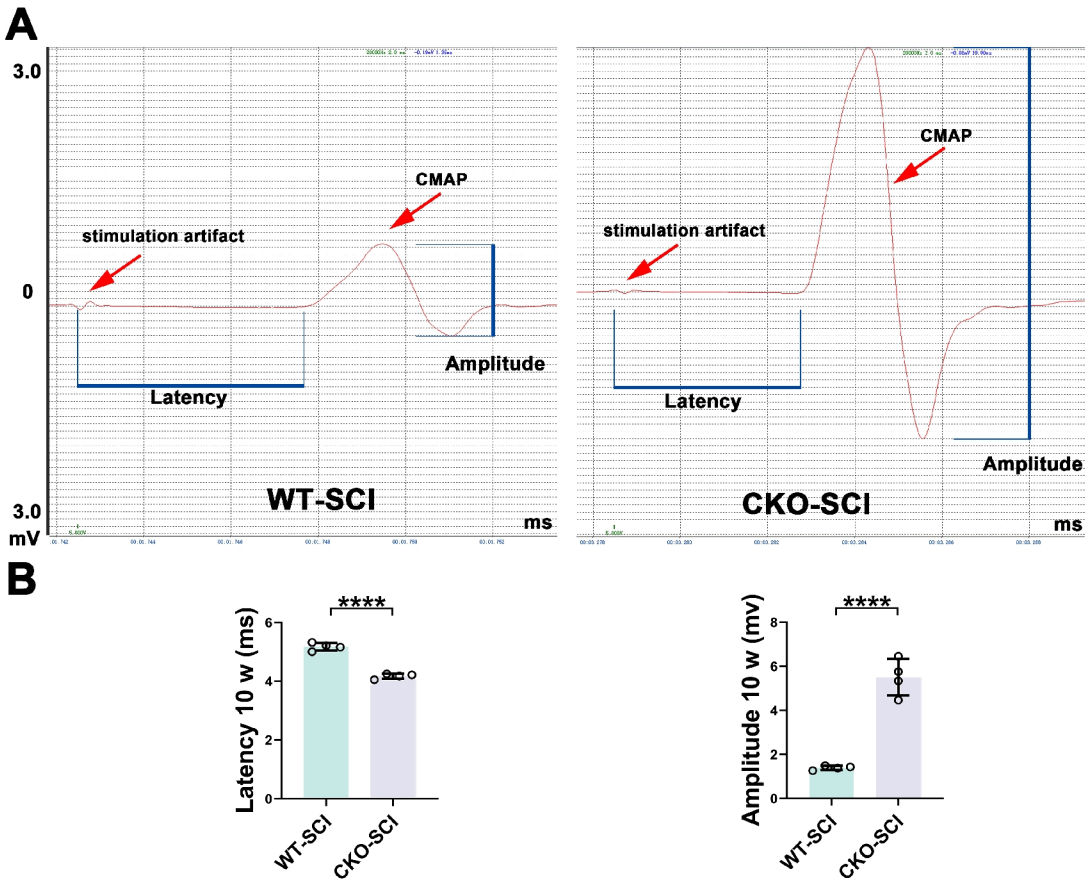

Figure S7. cKO-SCI mice exhibit improved electrophysiological function compared with WT-SCI controls. (A) Representative CMAP recordings from WT-SCI and CKO-SCI mice. (B) Quantification of CMAP latency and amplitude at 10 weeks post-injury. Data are mean ± SD; n = 4 mice/group; unpaired two-tailed *t*-test. Statistical significance: ****$p < 0.0001$.

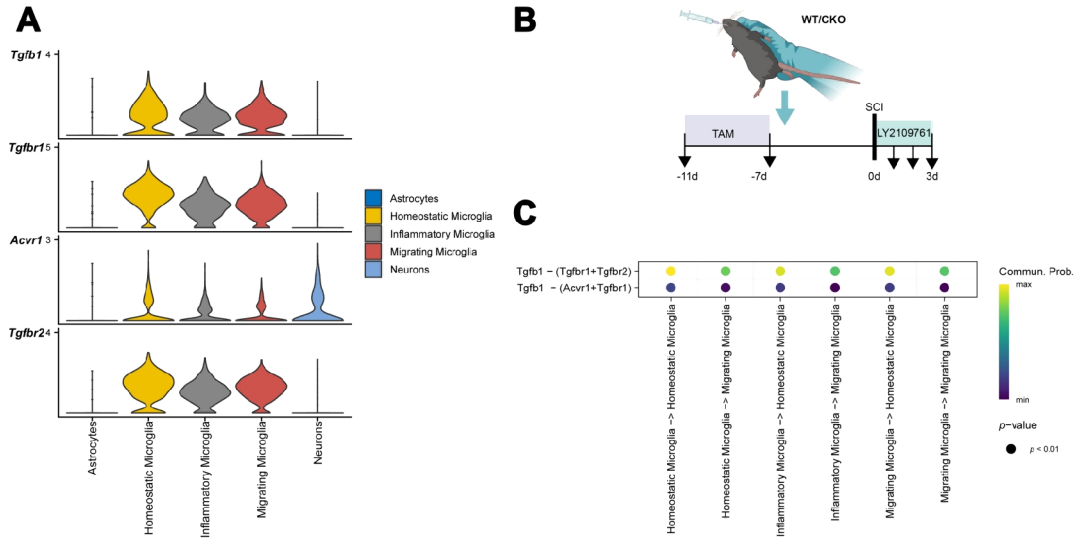

Figure S8. (A) Violin plots showing the expression levels of *Tgfb1* and its receptors (*Tgfbr1*, *Tgfbr2*, *Acvr1*) across major cell types. (B) Schematic diagram illustrating the experimental design for SCI and LY2109761 treatment. (C) Dot plot showing the communication probabilities of *Tgfb1-Tgfbr1*/*Tgfbr2* and *Tgfb1-Acvr1*/*Tgfbr1* ligand-receptor interactions among microglial subpopulations.

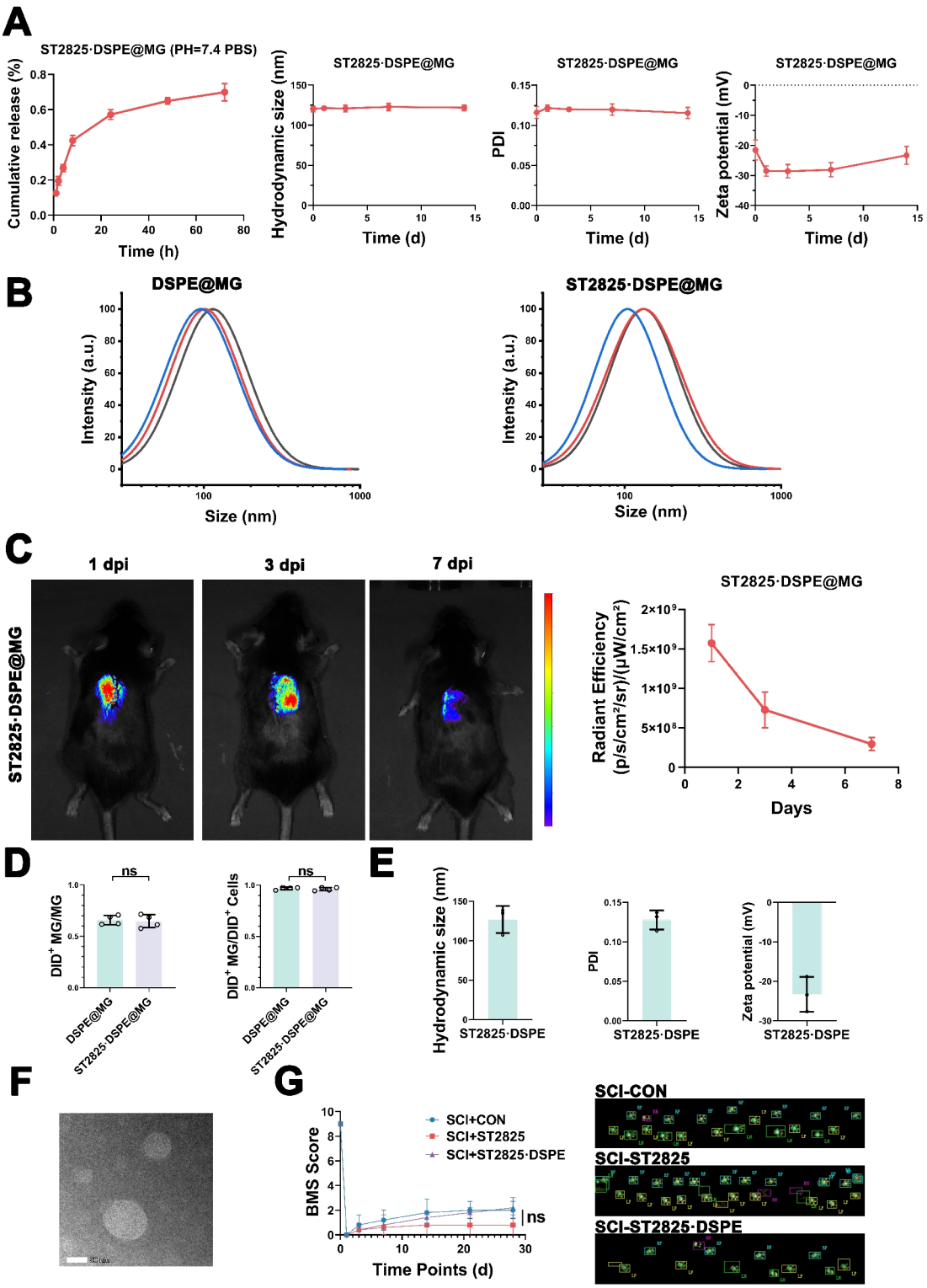

Figure S9. (A) *In vitro* drug release assays and colloidal stability tests of ST2825·DSPE@MG. (B) Size distribution of DSPE@MG and ST2825·DSPE@MG measured by DLS. (C) *In vivo* fluorescence imaging of DiD-labeled nanoparticles from 1 to 7 days post-administration, with quantification of radiant efficiency. (D)

Quantification of the DiD^+ cells in the perilesional region at 3 dpi. (E) DLS characterization of plain liposomes loaded with ST2825. (F) Representative TEM image of plain liposomes loaded with ST2825. Scale bars: 50 nm. (G) BMS scores and footprint analysis of the indicated groups. Data are mean ± SD; for (A, B, E), n = 3; for (C, D), n = 4 mice/group (unpaired two-tailed t-test for D). for (G), n = 5 mice/group (two-way repeated-measures ANOVA); ns, not significant.

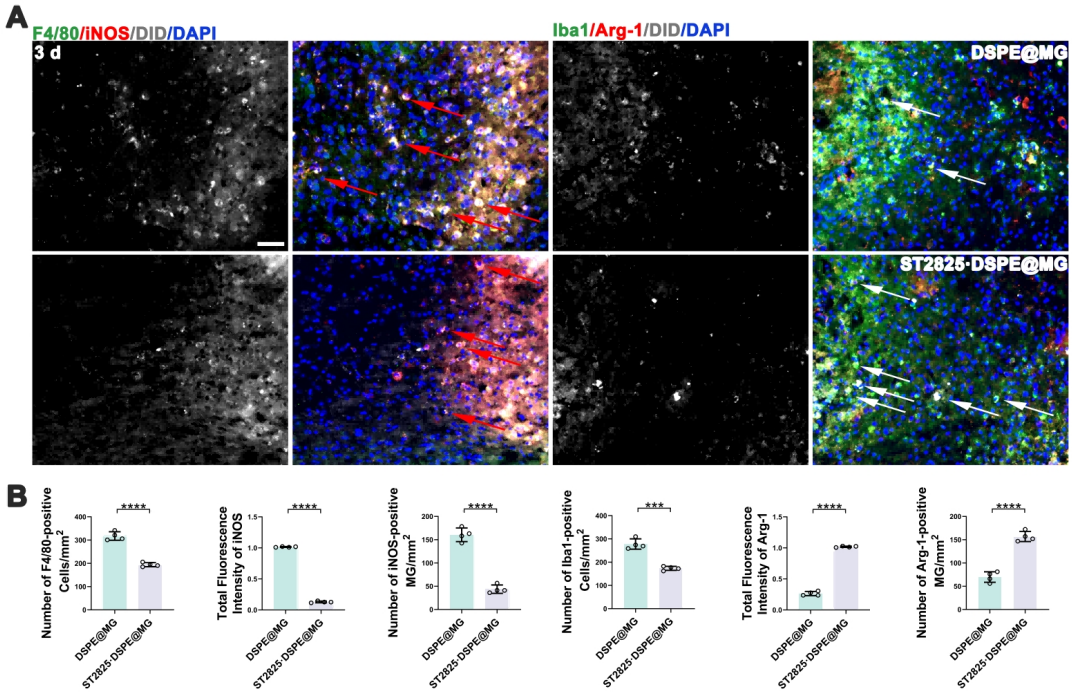

1168

1169 **Figure S10.** (A) Representative sections in the lesion area of male mice at 3 dpi

1170 stained for F4/80 (green) and iNOS (red), and Iba1 (green) and Arg-1 (red); DiD

1171 (white); DAPI (blue). (B) Quantification of lesion-region microglia and markers at 3

1172 dpi. Data are mean ± SD; n = 4 mice/group; unpaired two-tailed *t*-test. Scale bar, 50

1173 μm. Statistical significance: ***$p < 0.001$, ****$p < 0.0001$; ns, not significant.